

submitted to the *Astrophysical Journal*, April 1996

accepted, May 1996

COMPARISON OF VELOCITY AND GRAVITY FIELDS: THE MARK III TULLY-FISHER CATALOG VERSUS THE IRAS 1.2 JY SURVEY*

Marc Davis

Departments of Astronomy and Physics
University of California, Berkeley, CA. 94720, U.S.A
marc@coma.berkeley.edu

Adi Nusser

Institute of Astronomy, Madingley Rd, Cambridge, CB3 0HA, England
adi@ast.cam.ac.uk
and

Jeffrey A. Willick

Department of Physics, Stanford University, Stanford, CA 94305-4060
jeffw@perseus.stanford.edu

ABSTRACT

We consider a measure of the peculiar velocity field derived from the Mark III compilation of 2900 spiral galaxies (Willick *et al.* 1996b), using an analysis method that is substantially free of bias (Nusser & Davis 1995). We expand the velocity field in a set of orthogonal, smooth modes, reducing the data to a set of 56 coefficients fitted to a maximum redshift of 6000 km s^{-1} , and maximum spherical harmonic of $l = 3$. The radial resolution of the modes degrades with redshift, from 800 km s^{-1} locally to 3000 km s^{-1} at 4000 km s^{-1} redshift. Equivalent mode coefficients can be computed for the gravity field derived from any whole-sky redshift catalog of galaxies, such as the *IRAS* 1.2 Jy survey (Fisher *et al.* 1995). Given the coefficients of the expansions, one can compare the velocity and gravity fields on a galaxy by galaxy basis, or on a mode by mode basis. Detailed comparison shows the two independent fields to be remarkably aligned in general. There are, however, systematic discrepancies in the fields that lead to considerable coherence in the residuals between them. These residuals take the form of a dipole field in the LG frame that grows with distance; it is not consistent with a bulk flow residual.

We perform a likelihood analysis in the mode-mode comparison to determine which value of $\beta \equiv \Omega^{0.6}/b$ for the *IRAS* gravity field is the best fit to the Mark III velocity field, considering the errors and covariance in both the velocity and gravity coefficients. We find that the most likely value lies in the range $\beta = 0.4\text{--}0.6$. However, in contrast with results we obtain using simulated galaxy catalogs, the χ^2 per degree of freedom for the fit is well in excess of unity, primarily because of the coherent dipole residuals at $cz \gtrsim 3000 \text{ km s}^{-1}$. Thus, despite the general alignment of the Mark III velocity and *IRAS* gravity fields, they

* The manuscript with all its embedded figures (many in color) can be retrieved from <ftp://magicbean.berkeley.edu/pub/marc/m3itf/vitf.ps.gz>

do not agree in detail, precluding a firm determination of β from these data sets at present. The method is capable of measuring β to an accuracy of 10%, but without understanding these systematic discrepancies, we cannot infer a value of β from these data.

Subject headings: cosmology — dark matter — galaxies: clustering — galaxies: formation — gravity — large-scale structure of the universe

1. INTRODUCTION

The observed large scale flows of galaxies are a direct probe of the nature of the underlying dark matter in the Universe. Under the assumption that the large scale structure has formed via gravitational amplification of small initial density fluctuations, the observed velocity field yields a prediction for the present matter-density fluctuations given an assumed value for Ω (Nusser *et al.* 1991). Furthermore, quasi-linear gravitational instability theory can be used to reconstruct the primordial density fluctuations from the observed flows. This enables us to address fundamental questions about the nature of the initial fluctuations and their relation to Ω . For example, Nusser & Dekel (1993) have demonstrated that unless Ω is around unity the initial density fluctuations were non-gaussian.

The largest virialized systems in the Universe are the rare, rich clusters of galaxies, with typical sizes of less than $1 h^{-1}$ Mpc. The large scale flows, on the other hand, are motions with coherence length of order $10 - 40 h^{-1}$ Mpc, more than an order of magnitude larger than the rich cluster sizes. Measurements of mass by means of the alignment which is expected between velocity and gravity fields on these large scales is thus quite distinct from the virial, or hydrostatic, or weak lensing analyses that can be applied to the clusters. A trend of increasing mass to light ratio is well documented to exist with increasing scale size of the measurement (Ostriker *et al.* 1974, Davis *et al.* 1980). Rich clusters fall on this trend, with an inferred density parameter of order $\Omega_0 \approx 0.1 - 0.2$, consistent with the baryon fraction in the clusters (e.g. White *et al.* 1993). A fundamental question is whether the trend of Ω_0 versus scale asymptotes at this value, or continues to climb upward on larger scales. If galaxy formation is more efficient in denser regions or if galaxies have some degree of velocity bias, or if the dark matter is too hot to fully fall into the cluster potential wells, then we might expect to measure a larger value of Ω_0 on the scale of the large-scale flows. Considerations of an inflationary early Universe have traditionally led to the expectation of $\Omega_0 = 1$ (although see e.g. Liddle and Lyth 1993, Bucher and Turok 1995); our confidence in such speculations would be considerably enhanced if someone could actually produce compelling evidence, on any scale, to support such a high density.

On large scales, virial equilibrium does not apply, but one can still derive estimates of the mass density, now based on flow models, either linear or nonlinear. The earliest detailed flow models were based on Virgocentric infall (e.g. Aaronson *et al.* 1982, Tonry and Davis 1981). These models assumed a smooth background and spherical symmetry for the local supercluster, and this restrictive symmetry allowed the incorporation of nonlinearity in the relationship between velocity and density. We now know that spherical symmetry is a rather poor approximation for the infall to any cluster, but linear theory analysis, which assumes no special symmetry, remains a valid tool. The large scale flows are almost certainly the result of the process of gravitational instability (e.g. Dekel *et al.* 1993, but see Babul *et al.* 1994), with the overdense regions attracting material, and underdense regions repelling material. Initial conditions in the early universe might have been somewhat chaotic, so that the original peculiar velocity field (i.e. deviations from Hubble flow) was uncorrelated with the mass distribution, or even contained vorticity. But those components of the velocity field which are not coherent with the density fluctuations will adiabatically decay as the Universe expands, and so at late times one expects the velocity field to be

aligned with the gravity field, at least in the limit of small amplitude fluctuations. In this paper we shall attempt to make this comparison directly, using the best presently available data for both the velocity and gravity fields.

The subject of large scale flows has been extremely active of late, and two excellent reviews are now available (Dekel 1994; Strauss and Willick 1995). The observational situation is rapidly improving; in this paper we shall consider the velocity field derived from a sample of 2900 spiral galaxies with Tully-Fisher measurements (Willick *et al.* 1995; Willick *et al.* 1996a,b). The basic principle is to use late-time linear theory to relate the measured velocity field to the gravity field as predicted from the observed galaxy distribution. Given complete knowledge of the mass fluctuation field $\delta_\rho(\mathbf{r})$ over all space, one could trivially write the fluctuations in the gravity field $\mathbf{g}(\mathbf{r})$ as

$$\mathbf{g}(\mathbf{r}) = G\bar{\rho} \int d^3\mathbf{r}' \delta_\rho(\mathbf{r}') \frac{\mathbf{r}' - \mathbf{r}}{|\mathbf{r}' - \mathbf{r}|^3}, \quad (1)$$

where $\bar{\rho}$ is the mean mass density of the Universe. The great simplification of late time linear theory is the intuitive relation between the gravity field \mathbf{g} and the velocity field \mathbf{v}_L , namely $\mathbf{v}_L = \mathbf{g} t$ where the only possible time t is the Hubble time. The correct expression (Peebles 1980) is

$$\mathbf{v}_L(\mathbf{r}) = \frac{2}{3H_0\Omega^{0.4}}\mathbf{g}(\mathbf{r}). \quad (2)$$

If the galaxy distribution at least approximately traces the mass on large scale, with linear bias b between the galaxy fluctuations δ_G and the mass fluctuations (i.e. $\delta_G = b\delta_\rho$), then from (1) and (2) we have

$$\mathbf{v}_L(\mathbf{r}) = \frac{H_0\beta}{4\pi\bar{n}} \sum_i \frac{1}{\phi(r_i)} \frac{\mathbf{r}_i - \mathbf{r}}{|\mathbf{r}_i - \mathbf{r}|^3} + \frac{H_0\beta}{3}\mathbf{r}, \quad (3)$$

where \bar{n} is the true mean galaxy density in the sample, $\beta \equiv \Omega^{0.6}/b$, and where we have replaced the integral over space with a sum over the galaxies in a catalog, with radial selection function $\phi(r)$. ($\phi(r)$ is defined as the fraction of the luminosity distribution function observable at distance r for a given flux limit; see e.g. (Yahil *et al.* 1991).) The second term is the correction for the uniform component of the galaxy distribution which would exactly cancel the first term in the absence of clustering within the survey volume. One problem with Equation (3) is that the sum is to be computed in real space, whereas the galaxy catalog exists in redshift space. Furthermore, the integral is to be computed over all space, but the sum over the catalog must be truncated at some finite radius. Note that the result is insensitive to the value of H_0 , as the right hand side has units of velocity. We shall henceforth quote all distances in units of km s^{-1} . The density \bar{n} and selection function $\phi(r)$ can be estimated from the redshift catalog used in the analysis, so that comparison of the measured velocity field to the predicted velocity field $\mathbf{v}_L(\mathbf{r})$ gives us a measure of β . The degeneracy between Ω and b can be removed in principle by nonlinear effects (Nusser *et al.* 1991, Dekel *et al.* 1993), but in practice one should not be optimistic because, among other problems, nonlinear bias will enter at the same order as nonlinear velocity effects.

The direct comparison of the peculiar velocity of selected galaxies versus the gravity predicted from Equation (3) is fraught with difficulty. Distances to individual galaxies are typically uncertain at the level of 15-20% and are furthermore subject to considerable Malmquist bias. To compute the gravity field, one needs a nearly whole sky redshift catalog of galaxies. To date the best available catalog is the 1.2 Jy flux limited *IRAS* catalog of 5300 galaxies (Fisher *et al.* 1995), which we shall use in this analysis. The *IRAS* predicted gravity field has substantial uncertainty because of the dilute sampling of the density field. Furthermore, the predicted velocities are subject to large covariance, because the *IRAS* predicted field is quite non-local. Flows within the turnaround radius of large clusters are multivalued, so that in projection a given redshift can correspond to three separate distances. The examination of numerical simulations demonstrates that coherent shell crossing is a common occurrence near dense centers: the redshifts of a set of points can be larger (smaller) than the redshifts of nearby points with smaller (larger) distances. In this case, essential information has been lost and recovery of the correct distances from redshift information alone is impossible.

Several comparisons of velocity and gravity fields have been made with older datasets (e.g. Hudson 1994; Kaiser *et al.* 1991; Yahil 1988; Strauss and Davis 1988) but these analyses were all meant to be preliminary and none of their conclusions were compelling. To date nobody has included a proper treatment of the correlated noise in the analysis. Shaya *et al.* (1995) have compared the peculiar velocities of a set of 298 spiral galaxies within a redshift of 3000 km s^{-1} to the gravity field derived by least action analysis of the 1138 mass tracers derived from the *Nearby Galaxies Catalog* (Tully 1988). Their preliminary analysis gives a value $\Omega_0 = 0.2 \pm 0.2$, but they have not included covariance in the errors of the predicted mass model, nor have they realistically included possible influence from the mass distribution at redshifts $z > 3000 \text{ km s}^{-1}$, nor is it clear how well their analysis compares with the linear theory techniques used by others.

Because of the covariance of the *IRAS* gravity field a comparison of the mass fluctuations as inferred from the flows versus the *IRAS* density field has considerable merits. Assuming the flow is irrotational, the POTENT algorithm (Dekel *et al.* 1990) reconstructs a three dimensional flow from the observed radial flow field, and then computes derivatives of this flow to infer the underlying mass field (Nusser *et al.* 1991). This then can be compared directly to the *IRAS* density field (or to any other survey). Such a comparison was done by Dekel *et al.* (1993), using an earlier version of the *IRAS* catalog, and the Mark II catalog of peculiar velocities for 493 objects (Faber and Burstein 1988). On the basis of this density-density comparison, Dekel *et al.* (1990) derived $\beta = 1.3 \pm 0.3$. More recently, Hudson *et al.* (1995) have compared POTENT mass densities reconstructed from the Mark III data (Willick *et al.* 1995, 1996a, 1996b) with the optical density field of Hudson (1994), finding $\beta = 0.74 \pm 0.13$. A new analysis using the 1.2 Jy *IRAS* survey and the Mark III peculiar velocity catalog is in preparation (Dekel *et al.* 1996).

Given the significance of the questions raised, all viable alternative algorithms should be pursued to extract the implications of the large scale flows. In this paper we shall compare the observed radial velocity field with the radial gravity field inferred from the 1.2 Jy *IRAS* redshift survey (Fisher *et al.* 1995). We shall use the method of orthogonal

mode expansion as described by Nusser and Davis (1995), which we shall henceforth label as the Inverse Tully-Fisher (ITF) method. A disadvantage of the density-density comparison is that the mass-fluctuations which are derived by POTENT increase with decreasing β . According to the quasi-linear approximation (Nusser *et al.* 1991) employed by POTENT, the mass-fluctuation field inferred from the velocities diverges for low β , thus invalidating the density-density comparison. Therefore the density-density comparison can not formally rule out very low values of β . However, the fluctuations in the velocity field predicted from the observed distribution of galaxies are smaller for lower β and the applicability of the linear approximation is guaranteed. Therefore, the velocity-velocity comparison provides a better tool for assessing the agreement between the observations for low β .

This paper closely follows the methods described in Nusser and Davis (1994, hereafter ND94) and in Nusser and Davis (1995) (hereafter ND95), with some additional refinements developed since then (Davis and Nusser 1995). In Section 2, we review the essentials of these methods and describe our choice of basis functions. We also discuss the procedure for fitting the modes to both the velocity and gravity fields. As has been the case in the past, mock catalogs constructed from N -body simulations are essential for debugging and calibrating the methods. This is especially so for our application, since the entire analysis is performed in essentially pure redshift space. In Section 3, we show a few new details on the tests applied to the mock catalogs. Section 4 gives details of the comparison of the Mark III velocity field with the *IRAS* inferred gravity field, on a point by point basis, as well as on a mode by mode basis. A detailed likelihood analysis is presented in Section 5, where the needed covariance matrices are derived as well. Section 6 presents a discussion and final conclusions are given in Section 7.

2. Reconstruction of Peculiar Velocities

In this section we outline the methods of ND94 and ND95 for deriving the smooth peculiar velocities of galaxies from an observed distribution of galaxies in redshift space and, independently, from a sample of spiral galaxies with measured circular velocities $\eta \equiv \log \Delta v - 2.5$ and apparent magnitudes m . Any of the available methods (e.g. Yahil *et al.* 1991, Fisher *et al.* 1995b) for generating *IRAS* predicted peculiar velocities can be used. However, the method of ND94 is particularly convenient, as it is easy to implement, fast, and requires no iterations. Most importantly, this redshift space analysis closely parallels the ITF estimate described below. Since we shall use this analysis in what follows, we next present a very brief summary of the method.

2.1 Peculiar Velocities from the Distribution of Galaxies in Redshift Space

Let $\mathbf{v}(\mathbf{s})$ be the comoving peculiar velocity relative to the motion of the Local Group (LG) and \mathbf{s} the comoving redshift space coordinate. (We use $s = cz/H_0$, noting that higher order terms in z have a negligible influence on the derived velocity field). To first order, the peculiar velocity is irrotational in redshift space and it can be derived from a potential function, $\Phi(\mathbf{s})$, defined by $\mathbf{v}(\mathbf{s}) = -\nabla\Phi(\mathbf{s})$. Let $\delta_0(\mathbf{s})$ be the fractional fluctuation of the density field traced by the distribution of galaxies in redshift space. If we expand the angular dependence of Φ and δ_0 in terms of spherical harmonics (Fisher, Scharf & Lahav 1994, Fisher *et al.* 1995b) in the form, $\Phi(\mathbf{s}) = \sum_{l=0}^{\infty} \sum_{m=-l}^l \Phi_{lm}(s) Y_{lm}(\theta, \varphi)$ and similarly

for δ_0 , then, to first order, Φ_{lm} and δ_{0lm} satisfy,

$$\frac{1}{s^2} \frac{d}{ds} \left(s^2 \frac{d\Phi_{lm}}{ds} \right) - \frac{1}{1+\beta} \frac{l(l+1)\Phi_{lm}}{s^2} = \frac{\beta}{1+\beta} \left(\delta_{0lm} - \frac{1}{s} \frac{d \ln \phi}{d \ln s} \frac{d\Phi_{lm}}{ds} \right). \quad (4)$$

where ϕ is the selection function of the sample. As emphasized by ND94, the solutions to (4) for the monopole ($l = 0$) and the dipole ($l = 1$) components of the radial peculiar velocity in the LG frame are uniquely determined by specifying vanishing velocity at the origin. That is, the radial velocity field at redshift \mathbf{s} , when expanded to harmonic $l \leq 1$, is not influenced by material at redshifts greater than \mathbf{s} .

As an estimate of the field $\delta_0(\mathbf{s})$ from the discrete distribution of galaxies we consider,

$$\delta_0(\mathbf{s}) = \frac{1}{(2\pi)^{3/2} \bar{n} \sigma^3(s)} \sum_i \frac{1}{\phi(s_i)} \exp \left[-\frac{(\mathbf{s} - \mathbf{s}_i)^2}{2\sigma^2(s)} \right] - 1 \quad . \quad (5)$$

We emphasize that the coordinates \mathbf{s} are in *observed redshift* space, expanded in a galactic reference frame. The only corrections from pure redshift space coordinates is the collapse of the fingers of god of the known rich clusters prior to the redshift space smoothing (Yahil *et al.* 1991). The density field is here smoothed by a gaussian window with a redshift dependent width, $\sigma(s)$, which is proportional to the mean particle separation, i.e., $\sigma(s) \propto (\bar{n}\phi(s))^{-1/3}$, where \bar{n} is the mean density of the *IRAS* sample. The purpose of the smoothing is to limit the discreteness noise of the gravity field constructed from the dilute redshift sample. This particular smoothing ensures that the error in the field (5) due to Poisson noise is constant in space for the case of a uniform distribution of galaxies. A more elaborate realization of the density field based on Wiener filtering is described by Fisher *et al.* (1995b), with results very close to those obtained here. Weighting the galaxies in (5) by the selection function evaluated at their redshifts rather than the distances which are unknown yields a biased estimate for the density field and gives rise to Kaiser's rocket effect (Kaiser 1987). However, this bias should be compensated by the term involving the selection function in (4).

2.2 Peculiar Velocities from the Inverse Tully-Fisher relation: Expansion of the Fields in Orthogonal Functions

Given a sample of galaxies with measured circular velocity parameters, η_i , apparent magnitudes, m_i , and redshifts, z_i , the goal is to derive an estimate for the smooth underlying peculiar velocity field. We assume that the circular velocity parameter, η , of a galaxy is, up to a random scatter, related to its absolute magnitude, M , by means of a linear inverse Tully-Fisher (ITF) relation, i.e.,

$$\eta = \gamma M + \eta_0. \quad (6)$$

The advantages of inverse TF methods were first described in detail by Schechter (1980) and Aaronson *et al.* (1982). Most critically, samples selected by magnitude, as most

are, will not be plagued by Malmquist bias effects when analyzed in the inverse direction. Methods based on an inverse relation generally require a velocity model (Schechter 1980, Aaronson *et al.* 1982, Lynden-Bell 1991, Lahav 1991) which can be parameterized in terms of observable redshifts. ND95 consider a very general model and write the absolute magnitude of a galaxy, $M_i = M_{0i} + P_i$, where $M_{0i} = m_i + 5\log(z_i) - 15$ and $P_i = 5\log(1 - u_i/z_i)$, where m_i is the apparent magnitude of the galaxy, z_i is its redshift in units of km s^{-1} , and u_i its radial peculiar velocity in the LG frame. In general, one can write the function P_i in terms of an expansion over orthogonal functions,

$$P_i = \sum_{j=0}^{j_{max}} \alpha^j \tilde{F}_i^j \quad (7)$$

with orthonormality conditions,

$$\sum_{i=1}^{N_g} \tilde{F}_i^j \tilde{F}_i^{j'} = \delta_K^{j,j'}, \quad (8)$$

with the zeroth mode defined by $\tilde{F}_i^0 = 1/\sqrt{N_g}$, where N_g is the number of galaxies in the sample. The zeroth mode describes a Hubble-like flow in the space of the data set which is clearly degenerate with the zero point of the ITF relation. Here we arbitrarily set $\tilde{\alpha}^0 = 0$. The best fit parameters, α^j , the slope, γ , and the zero point η_0 , are found by minimizing the χ^2 statistic

$$\chi^2 = \sum_i \frac{(\gamma M_{0i} + \gamma P_i + \eta_0 - \eta_i)^2}{\sigma_\eta^2}. \quad (9)$$

where σ_η is the *rms* scatter in η about the ITF relation. With our choice for the zeroth mode, the solution for α^j is,

$$\begin{aligned} \alpha^j &= -\frac{1}{\gamma} \sum_i (\gamma M_{0i} - \eta_i) \tilde{F}_i^j, \\ \gamma &= \frac{\sum_{i,i'} M_{0i} \eta_{i'} \left(1 + N_g \sum_j \tilde{F}_i^j \tilde{F}_{i'}^j\right) - N_g \sum_i M_{0i} \eta_i}{\sum_{i,i'} M_{0i} M_{0i'} \left(1 + N_g \sum_j \tilde{F}_i^j \tilde{F}_{i'}^j\right) - N_g \sum_i M_{0i}^2}. \end{aligned} \quad (10)$$

As described in ND95 the choice of radial basis functions for the expansion of the modes can be made with considerable latitude. The functions should obviously be linearly independent, and close to orthogonal when integrated over volume. They should be smooth and close to a complete set of functions up to a given resolution limit. ND95 chose spherical harmonics Y_l^m for the angular wavefunctions and the derivatives of spherical Bessel functions for the radial basis functions, motivated by the desire to use functions which automatically satisfy potential theory boundary conditions at the origin and the outer boundary. That is, they chose

$$P(z, \theta, \phi) = \sum_{n=0}^{n_{max}} \sum_{l=0}^{l_{max}} \sum_{m=-l}^{m=l} \frac{a_{nlm}}{z} (j_l'(k_n z) - c_{l1}) Y_{lm}(\theta, \phi) \quad . \quad (11)$$

The constant c_{l1} is non-zero for the dipole term only and ensures that $P = 0$ at the origin, and is non-zero at the outer boundary. Details of how the orthogonalized functions \tilde{F}_i^j are derived from this expansion are given in ND95.

To keep the expansion of the basis functions compact, it is sensible to match the resolution of the wavefunctions to the spatial distribution of the Tully-Fisher data. Since the precision of the inferred peculiar velocities is a constant fraction of the distance to any galaxy, spherical Bessel functions, which oscillate uniformly with their argument, are not the optimal choice of wavefunction. Furthermore, the mean interparticle spacing of galaxies in flux limited redshift catalogs, from which we infer the density and gravity fields, can increase even more rapidly than linearly with distance. For example, for $z \gg 6000 \text{ km s}^{-1}$, the mean interparticle spacing within the 1.2 Jy *IRAS* survey increases as $z^{1.6}$. Therefore, to make optimal use of the available information from the ITF field, we expand the modes of P_i in terms of a transformed radial coordinate that decreases the oscillation periods of the Bessel functions roughly according to the distribution of data as a function of redshift. A convenient, but by no means unique choice is

$$y = (\ln [1 + (z/z_*)^2])^{1/2} . \quad (12)$$

For an increment Δy , this function has resolution $\Delta z = (dy/dz)^{-1} \Delta y$ that is constant on small scale and $\Delta z \propto z \ln(z)$ on large scale. We set $z_* = 1000 \text{ km s}^{-1}$. The radial wavenumbers for each l value have been chosen for the lowest values of k_n such that

$$j_{l-1}(k_n y_{max}) = 0 . \quad (13)$$

This choice does not restrict the value of the expanded velocity field near the boundary y_{max} . As we shall see, transforming to the variable y results in a significant reduction in the value of the χ^2 of the fit relative to the expansion in terms z . Given these choices of radial variable and values of k_n , the resulting wavefunctions for $l = 0, 4$ are plotted in Figure 1. Note how the wavelength of the modes increases with distance. All of the modes are forced to be orthogonal to the $P = constant$ mode when summed over the set of points in the Mark III catalog, and this is accomplished by small additive constants. However, the $n = 1, l = 0$ mode is positive definite over the volume, and to make it orthogonal to the $P = constant$ mode would require a substantial additive offset, which would then violate the proper boundary condition at the origin. We therefore delete this mode from inclusion in our expansion set.

As a demonstration of the use of the variable y , we tested the Mark III catalog which lists 2237 galaxies within $s = 6000 \text{ km s}^{-1}$, details of which will be described below. We took the linewidth scatter to be $\sigma_\eta = 0.05$ (Willick *et al.* 1995). For no velocity model, (i.e. setting all coefficients $\alpha^j = 0$), the scatter diagram of the Tully-Fisher regression of observed versus predicted linewidths η yields $\chi^2 = 3516$. Fitting a flow model of 69 degrees of freedom ($l_{max} = 3, n_{max} = 4$) in terms of radial wavefunctions $j'_l(k_n z)/z$ leads to a much reduced $\chi^2 = 2667$, while doing the same fit of 69 modes in terms of $j'_l(k_n y)/z$ gives $\chi^2 = 2644$, a modest but significant improvement. Further tests on simulations with smaller σ_η demonstrate that the effect of the coordinate transformation is considerably

more pronounced. There is clearly room for refinement here, but this choice of radial variable is sufficient for our purposes, especially since we shall use identical basis functions for the expansion of the velocity and gravity fields.

2.2.1 Choosing the resolution limit

In the comparison of the Mark III velocity and *IRAS* gravity fields discussed below, we shall use the Mark III sample only within a redshift limit of 6000 km s^{-1} . This corresponds to setting the outer boundary condition at $y_{max} = 1.9$. If we consider that the number of peaks in the n th radial wavefunction is n , then the effective resolution R at any redshift is $R(z) \approx \left(\frac{dy}{dz}\right)^{-1} \frac{y_{max}}{n}$. For $n_{max} = 4$, $z_{max} = 6000 \text{ km s}^{-1}$, and $z_* = 1000 \text{ km s}^{-1}$, the resulting limiting radial resolution is 680 km s^{-1} at $z = 1000 \text{ km s}^{-1}$, and 3400 km s^{-1} at $z = 4000 \text{ km s}^{-1}$.

The angular resolution for a spherical harmonic function Y_{lm} is $180/l$ degrees. For redshift z , this corresponds to a maximum spatial resolution of $R \approx \pi z/l_{max}$. If we desire to have the angular and physical resolutions approximately equal at 3000 km s^{-1} , where the radial resolution is approximately 2400 km s^{-1} , then we should select $l_{max} = 3.9 \approx 4$. We shall in fact limit l_{max} to 3, in order to reduce the number of degrees of freedom. The result is that our radial resolution is slightly higher than our transverse resolution, but by our choice of radial variable y , the ratio of transverse to radial resolution is approximately constant with distance, which is a desirable feature.

The choice of the variable y is governed by the desire to have a mode resolution that is a fixed fraction of the resolution of the TF data, but as long as the resolution is below that of the intrinsic data, we can be assured that both the smoothed velocity and gravity fields have identical resolution. We have chosen a mode resolution corresponding to the spatial frequency of the fourth dipole mode: $k = \frac{4\pi}{y_{max}}$. That is, we include the first 4 radial modes that satisfy the outer boundary condition, equation (13), for the harmonic $l = 1$. We use this limiting cut in wavenumber as a limit for the other spherical harmonics. Thus to the same limiting value of k , we should include 4 modes for $l = 0$, the first of which is discarded, 3 modes for $l = 2$, 3 modes for $l = 3$, 2 modes for $l = 4$, 2 modes for $l = 5$, and 1 mode for $l = 6$. However, tests based on the efficiency of the decrement in the χ^2 value of the fit demonstrated that a cutoff in l is desirable here. Thus on top of the sharp cutoff in k -space we eliminate modes with harmonic index exceeding $l_{max} = 3$, as mentioned above. This yields $3 \times 1 + 4 \times 3 + 3 \times 5 + 3 \times 7 + 5 = 56$ modes in total. The Mark III velocities within a limiting redshift of 6000 km s^{-1} were then derived from the ITF method. The peculiar velocities as predicted from the *IRAS* real or mock catalogs were expanded in the same ITF basis functions, as described next.

2.2.2 Expanding the *IRAS* velocity field

Using the machinery for computing a gravity field described in §2.1, one can generate a linear theory predicted peculiar velocity v_L for any point in space as a function of its redshift for any value of β . We must ensure that the smoothing scales of the ITF

and *IRAS* predicted peculiar velocities are matched to the same resolution. Therefore we expand v_L in terms of the modes used in the velocity model (12). Because of the orthonormality, we can write the mode coefficients as

$$\alpha_{iras}^j = 5 \sum_i \log \left(1 - \frac{(v_{Li} - H' z_i)}{z_i} \right) \tilde{F}_i^j, \quad (14)$$

where the H' term is a correction for Hubble flow and the summation index i is restricted to be over the positions of the same galaxies in the ITF expansion.

This procedure will filter out higher frequency modes that are not described by the resolution of our basis functions. However, it is important to recall that the modes are chosen to be orthogonal to the mode $P_i = \text{constant}$, which would describe a smooth Hubble flow. In the fitting for the ITF modes, pure Hubble flow is absorbed into a shift of the zero point η_0 and the orthogonality is ensured. Within a given set of test points occupying a volume smaller than that used to define the gravity field, it is possible for v_L to have a non-zero value of Hubble flow H' , which must be removed from v_L before we tabulate the mode coefficients. That is, we tabulate the mean Hubble ratio

$$H' = \frac{1}{N} \sum_i \frac{v_{Li}}{z_i} \quad (15)$$

and subtract it from the predicted field v_L . This “breathing mode” which mimics a Hubble flow is not trivial in amplitude, and can be a 10% correction on the effective Hubble constant within simulated catalogs.

3. Tests with Mock Catalogs

ND94 and ND95 tested the velocity reconstruction methods and their biases using mock catalogs drawn from an N -body simulation of a CDM, ($h = 0.5$, $\Omega_0 = 1$, and $\sigma_8 = 0.7$) universe. The simulation had the disadvantage of having low amplitude large scale flows and therefore was not fully suitable for our purposes. Furthermore, the algorithm for attenuating the rather large small-scale incoherent velocities seen in the simulation resulted in too much reduction of their amplitude. Here we provide more powerful tests of the methods using mock Mark III and 1.2Jy *IRAS* catalogs which are extracted from a pure $n = -1$, $\Omega_0 = 1$ simulation of 10^6 points kindly supplied by S. White. We use a normalization $\sigma_8 = 0.7$, which then determines that the size of the box is $L = 235h^{-1}$ Mpc. Such a simulation has the desirable feature of having very high-amplitude large scale flows. In this simulation, as in the CDM simulation used in ND, the one-dimensional small scale (few Mpc scale) velocities are far in excess of that observed for the real universe ($\approx 140 - 200 \text{ km s}^{-1}$; see Miller *et al.* 1996) and have to be smoothed somehow. Instead of replacing the N -body peculiar velocities with Gaussian smoothed velocities as we have done in previous work (Fisher *et al.* 1993), we replace the original N -body velocities with the average of a Gaussian smoothed field (with smoothing length $\sigma = 100 \text{ km s}^{-1}$) and the original field. Thus we reduce the one dimensional RMS amplitude of the very small scale velocity field σ_u from 400 to 200 km s^{-1} while keeping the large scale velocities unchanged.

This is of course not a self-consistent procedure, but better approximates the observations and the expected effects of possible velocity bias, or of baryon dissipation within extended dark matter halos. In dense regions, with $\bar{\delta} > 600$, we collapse the redshift space fingers of god, as is done in the centers of real clusters for both the Mark III and *IRAS* catalogs.

In order to generate realistic mock catalogs from the simulation, a particle moving at 600 km s^{-1} , with small local shear, and which is not in a dense region is chosen as the central observer. A mock full sky 1.2Jy *IRAS* catalog is generated from the simulation by assigning luminosities to particles according to the luminosity function of the 1.2Jy *IRAS* survey. This procedure results in 5021 “galaxies” out to a redshift of $180h^{-1}\text{Mpc}$ from the “observer”.

To select mock Mark III catalogs, we follow the procedure described in ND95, with the following modifications: we extract a nonuniform subset of points from the mock *IRAS* catalogs, with galaxies at $|b| < 18^\circ$ heavily selected against, and with objects in the hemisphere of the microwave dipole anisotropy vector having twice the probability of selection as objects in the anticenter direction. Each point within the mock catalog has an absolute magnitude drawn from the luminosity function of the 1.2 Jy *IRAS* catalog. The selected points in the mock Mark III sample are given a linewidth η drawn from a linear Tully-Fisher law with $\eta_0 = -2$ and $\gamma = -0.1$, and with gaussian scatter $\sigma_\eta = 0.05$, a value we find to closely fit the observed scatter in the real Mark III catalog. The mock Mark III data thus consist of a position on the sky, a redshift, apparent magnitude, and linewidth for each galaxy; the true peculiar velocity of each “galaxy” is used only to test the reliability of the reconstruction. A much more elaborate construction of mock Mark III catalogs is described by Kolatt *et al.* (1996). We have tested our procedures on this catalog for which we have no more difficulty recovering the true underlying field than with the mock catalogs described here.

With these two catalogs, we can generate mock ITF velocity fields as described above, and mock *IRAS* velocity fields using the technique of ND94 described above. By simply changing the random number seed, we have generated different realizations of the mock Mark III sample for the same points, and different mock *IRAS* catalogs from the same central observer within the N -body simulation.

To generate the mock *IRAS* velocity field by means of the method described in Section 2.1, we first use the unbiased “galaxy” distribution out to 18000 km s^{-1} to generate a smooth density field. We fix the Gaussian smoothing length $\sigma(s)$ to be the mean particle separation at the redshift s . For the 1.2 Jy *IRAS* catalog, this smoothing is approximately $\sigma(s) = 345 \text{ km s}^{-1}$ at $z = 1000 \text{ km s}^{-1}$, $\sigma(s) = 570 \text{ km s}^{-1}$ at $z = 3000 \text{ km s}^{-1}$, and $\sigma(s) = 980 \text{ km s}^{-1}$ at $z = 6000 \text{ km s}^{-1}$, considerably smaller than the mode filtering we shall apply to the ITF velocity and *IRAS* gravity fields, but large enough to filter out many of the nonlinear structures in the mock *IRAS* catalog. The density field and resulting velocity field (equations 4 and 5) are then expanded in spherical harmonics up to $l_{max} = 12$, although in fact a lower cutoff at $l = 4$ is sufficient. Using this relatively high resolution velocity field based on the mock *IRAS* catalog, we generate a linear theory prediction for each point in the mock Mark III catalog.

We use the 56 mode expansion to minimize the scatter of the Tully-Fisher relation in the mock Mark III catalog; for the 1733 points in the mock catalog within $s = 6000$ km/s, the χ^2 of the fit is reduced from 2264 with no flow, to 1900 with a 56 mode flow model. Note that the reduced χ^2 is somewhat greater than unity in spite of our precise knowledge of the scatter in η . The slightly high χ^2 is simply due to components of the velocity field with higher spatial frequency than the resolution of our mode expansion; however, increasing the number of modes in the expansion reduces χ^2 relatively slowly. If the η scatter were smaller, more degrees of freedom would be worthwhile. We recover best values of $\eta_0 = -1.94$ and $\gamma = -0.0965$, only slightly off their input values of -2.0 , -0.1 .

We find it most useful to present the results of the flow model pictorially. In Figure 2 we present three redshift slices of the ITF velocity field u_{itf} derived for the mock catalog using the 56 mode expansion. The plots are in galactic coordinates where stars (circles) represent mock galaxies outflowing (inflowing) in the LG frame, with sizes proportional to the flow amplitude. In Figure 3 we show u_{itf} projected onto the Supergalactic Plane. Note that although the data are irregularly distributed, the velocity field is very smooth, by construction. These plots, like all the plots in this paper, are in the Local Group frame. Note the strong reflex dipole signature which dominates the large scale flow.

The real advantage of working with mock catalogs derived from self-consistent N -body simulations is that for each point we know the true peculiar velocity u_{true} , including all the nonlinear, small scale effects. Figure 4a shows the true, unfiltered velocity field u_{true} of the mock Mark III points, projected to the supergalactic plane, while Figure 4b shows the true field after filtering by the ITF mode functions u_{true}^f , Equation (14). Note how the region of substantial shell crossing shown near the clusters of the upper left section of Figure 4a is largely eliminated in the filtered version of the field, Figure 4b. Figure 4c shows the *IRAS* derived, unfiltered velocities u_{iras} , while Figure 4d shows the *IRAS* derived velocities after filtering, u_{iras}^f . The u_{true} field has a dipole signature on large scale, and considerable complex structure around the dense knots; the u_{iras} field is considerably smoother and cleanly separates the infalling and outflowing zones, particularly in the upper left portion of Figure 4c, as expected from a Zeldovich approximation methodology. Note that Figures 3, 4b, and 4d, the smoothed versions of the ITF, true, and *IRAS* fields, are all very similar, indicating that the ITF process does recover the true peculiar velocity field, as does the *IRAS* gravity field. The similarity of Figure 4c to 4d demonstrates that the 56 mode filtering recovers most of the information contained within the *IRAS* predicted flow field. The higher resolution velocity information of the unfiltered *IRAS* flow field has relatively low amplitude in most regions.

To be slightly more quantitative, we present in Figure 5a the residual $u_{itf} - u_{true}^f$ as a function of z , with points within 60 degrees of the apex angle toward ($l = 270$, $b = 30$) plotted on the right, and those within 60 degrees of the antiapex plotted on the left. Note that there is a slight monopole residual, with all distant points having slightly negative residuals. This has resulted from bias in the determination of the Tully-Fisher slope γ , which has been fit by the χ^2 minimization procedure but has led to a biased estimate, $\gamma = -0.0965$, instead of the correct value $\gamma = -0.1$. The bias has been induced by the thermally “warm” velocity field of the mock Mark III catalog, as expected (see ND95 for

further details). If instead of allowing γ to be determined by the χ^2 minimization, we fix it at its correct value, the resulting χ^2 increases from 1900 to 1905, but the resulting field has no residual monopole, as shown in Figure 5b. Figures 2-4, as shown, were corrected for this bias. We can expect a similar bias for the real data, since the scatter in σ_u has approximately the same amplitude as the mock catalog, and we shall therefore correct the measured TF slope by the same factor of 3.5%. This bias is so minor that none of the results to follow are affected if we ignore it altogether.

Having corrected for this bias, we next examine maps of the residual fields. Figure 5c shows the residuals $u_{itf} - u_{iras}^f$, plotted in the same manner as Figure 5ab. Note that the residuals are now somewhat larger and increase with distance, but show no systematic offsets. Figures 6a and 6b show the residuals $u_{itf} - u_{true}^f$ and $u_{itf} - u_{iras}^f$ plotted in slices of the full sky. Note that the amplitude of Figure 6b is larger than in Figure 6a, showing that *IRAS* induced errors are a major contributor to the errors in the procedure. Note again that all the errors are coherent, as expected since the field is limited to $l = 3$; neither the velocity nor gravity field contain any information at higher resolution. Comparison of different mock *IRAS* and mock Mark III catalogs shows similar coherence in the residuals, but largely differing sky patterns than shown in Figure 6b. An important point to emphasize for what follows is that the dipole component of the error in the mock catalogs is small; the errors appear to be largely dominated by higher multipoles. The coherence of the residuals makes it difficult to judge the adequacy of the fit, but we shall see below when we consider the statistics of the mode amplitudes that these fits are consistent with the expected noise.

4. Comparison of Mark III vs *IRAS*

Having set the stage by means of the mock catalogs, we now consider the actual comparison of the ITF velocity field from Mark III and the gravity field derived from the *IRAS* 1.2 Jy catalog. Although the agreement between the mock Mark III and the mock *IRAS* catalogs was outstanding, we shall find that the comparison of the true velocity and gravity fields is considerably more problematic.

4.1 Preparation of the Mark III Database

Before constructing the ITF velocity field, it is necessary to bring the Mark III data to a uniform linewidth and magnitude system. In its raw form, the catalog consists of six distinct pieces, each with its own TF relation (Willick *et al.* 1996a), but by means of direct comparison of overlapping galaxies, the catalog can be standardized. We briefly summarize the procedure here; complete details are given by Willick *et al.* (1996b). Note that we use only spiral galaxies in the present analysis.

We assume that all six Mark III samples can be placed on a “common system” by linearly transforming the apparent magnitudes and velocity widths, or TF *observables*. For the reasons discussed by Willick *et al.* (1995), the Han-Mould (HM) cluster sample was used as the template data set, i.e., the HM data are unchanged in our analysis. The remaining samples are then transformed via a hierarchical overlap-comparison procedure

analogous to that described by Willick *et al.* (1996a), except that now the TF observables rather than the TF distances are required to agree in the mean with those of the same objects appearing in already-transformed samples. Transformations of the form

$$\eta_{\text{common}} = a_{0,S} + a_{1,S}\eta_S + a_{2,S}\eta_S^2 \quad (16)$$

and

$$m_{\text{common}} = m_S + b_{0,S} + b_{1,S}(m_S - 5 \log cz) \quad (17)$$

are fitted to the overlap data (with one exception, discussed in the next paragraph), where the subscript “*S*” denotes a given sample, and “common” refers to the values of the observables on the “common system” ultimately adopted for our analysis. The quadratic coefficient $a_{2,S}$ was non-zero only in the case of the Courteau-Faber (CF) sample, while the coefficient $b_{1,S}$, which represents a luminosity dependence of galaxy color, is non-zero only in the case of the *H*-band Aar onson *et al.* (A82) sample. Values of all coefficients that appear in equations (15) and (16) are tabulated by Willick *et al.* (1996b).

For the Mathewson *et al.* (1992; MAT) sample, we adopted a modification to Equation (15). When the MAT η ’s were initially transformed to the common system, the fit residuals correlated weakly with redshift, in the sense that higher redshift MAT objects appeared to have smaller widths than those of the same objects in other samples. A possible interpretation is that the MAT widths, which were measured chiefly in the 21 cm line at lower redshifts, but primarily optically in the $H\alpha$ line at higher redshifts, are biased low with increasing redshift. To account for this possibility, we tried a transformation of the form

$$\eta_{\text{common}} = a_{0,\text{MAT}} + a_{1,\text{MAT}}\eta_S + a_{3,\text{MAT}} \log(cz). \quad (18)$$

This yielded a coefficient $a_{3,\text{MAT}} = 0.065 \pm 0.025$, which is small but statistically significant, and a small but significant decrease in the scatter of the overlap comparison. We subsequently found that the ITF velocity fit using the MAT widths transformed according to (17) produced a significant reduction in the ITF χ^2 statistic. We have therefore adopted the redshift-dependent transformation (17) for the MAT sample throughout the analysis presented in this paper; we discuss possible implications of this further in § 6.

A final step in the preparation of our modified Mark III sample involves the rejection of outliers. As has been noted elsewhere (e.g., Willick *et al.* 1996a), the TF residuals of typical complete samples are not strictly Gaussian. Rather, they tend to consist of a gaussian core plus a small (1–2%) admixture of 4–5 σ outliers. Such objects are not helpful to velocity analyses, as they vitiate the assumption of Gaussianity that underlies almost all statistical methodologies. In our study we purged such points in the following way. First, we fit a bulk flow model to the entire sample. We computed the scatter σ_η from this fit, and then eliminated the 29 objects which deviated by more than $3.3\sigma_\eta$. These rejected galaxies were distributed throughout the volume of the MAT sample. When we refitted the bulk flow models, the scatter was reduced by 10% as a result of this small pruning of the sample, while the direction and amplitude of the bulk flow were essentially unchanged. Moreover, there were no remaining points which deviated by $\geq 3.3\sigma_\eta$ relative to the reduced scatter. Thus, our exclusion procedure resulted in a statistically improved

(i.e., more gaussian) sample, without significantly altering the global properties of the velocity field the sample produces.

4.2 Maps and Residuals of the Real Sky

The first stage is to fit the Tully-Fisher data of Mark III to the 56 orthogonal modes. For 2237 galaxies with $cz < 6000 \text{ km s}^{-1}$, the χ^2 of the TF regression drops from 3362 to 2616 when all the modes are included, assuming a scatter of $\sigma_\eta = 0.05$. The η scatter of the different pieces of Mark III is not identical, but the observed η scatter after fitting the modes is spatially random, so a nonuniformly weighted fit will be unchanged from the present procedure. When a 3.5% correction is made to unbiased the slope of the TF regression, to $\gamma = -0.112$, the χ^2 increases to 2623, which is statistically significant, but the resulting flow field is negligibly changed. The derived TF slope is 2σ deviant from the slope derived by the inverse fits for the Han-Mould sample, $\gamma = -0.1177 \pm 0.0025$ (Willick *et al.* 1995, 1996a), but this slope is derived with a very different flow model, so we consider the agreement satisfactory.

Note that the resulting χ^2 per degree of freedom is 1.15, significantly greater than unity. The excess fluctuations are primarily caused by small scale velocity fields and multi-valued zones with coherence scale below the resolution of the mode expansion. This is a slightly higher reduced χ^2 than obtained with the mock catalog, and the increased χ^2 could be due to slight deviations from Gaussianity in the Tully-Fisher scatter of the Mark III catalog, an effect we did *not* include within the mock catalogs. Our pruning of outliers from the Mark III catalog was very modest.

We have examined plots of the distribution of $\delta\eta$ in redshift and on the sky; all the plots are uniformly random. In Figure 7 we show the correlation function of the η residuals (see e.g. Gorski *et al.* 1989), before and after the modal expansion. This plot demonstrates the residuals to have zero coherence on scales larger than the resolution scale of the mode expansion. It appears as though the mode expansion has done its job; the expansion of P_i in a set of smooth functions has greatly reduced the scatter of the inverse TF diagram. The randomness of the $\delta\eta$ scatter suggests that the 56 mode expansion is sufficient for this dataset. With a larger dataset and/or more precise distance indicators, a larger set of expansion coefficients would be justified.

The resulting ITF velocity field of the Mark III galaxies is shown in slices of redshift space in Figure 8, and projected onto the Supergalactic plane in Figure 9. Both of these velocity maps are in the Local Group frame. In the nearby zone, the flow is dominated by infall to Virgo ($l = 284^\circ$, $b = 74^\circ$) and Ursa Major (145° , 65°) in the North, and modest outflow from Fornax (237° , -54°) in the south. In the middle redshift zone, the dipole pattern persists, and is more pronounced. This is composed partially by reflex dipole of the motion of the LG, plus backside infall from behind the Virgo supercluster. The Hydra cluster seen at (270° , 26°) is observed to be falling toward us, while the foreground of the Centaurus region (310° , 20°) is moving away from us. In the most distant slice of redshift space, the dipole pattern is further enhanced, with the entire Southern galactic sky, including the Perseus-Pisces region (150° , -15°) and the Pavo-Indus-Telescopium

region (320° , -15°) flowing away from us, the Centaurus cluster flowing away rather substantially, but the background of Hydra and the Northern galactic cap flowing toward us. All of this is a combination of the reflex of the motion of the LG, plus the motion of the individual regions. Note the very strong shear in the observed ITF field along the boundary $l = 300$, $b > 0$, which divides the Hydra and Centaurus regions, and amounts to a change of radial peculiar velocity of approximately 900 km s^{-1} in a transverse interval of 4100 km s^{-1} , or 20% of a Hubble flow differential motion over a substantial volume! This is quite a major gradient, one that appears to have been confirmed by distance estimates of elliptical galaxies in Centaurus (Lynden-Bell *et al.* 1988, Dressler 1994). In fact the true gradient is limited by the angular resolution of our modal expansion, since the reported outflow of the Centaurus clusters is $500\text{--}2000 \text{ km s}^{-1}$ in the LG frame, whereas the ITF measured flows for the entire Centaurus cluster are in the range $350\text{--}450 \text{ km s}^{-1}$ in the LG frame.

For comparison, we show in Figure 10 the *IRAS* predicted field for $\beta = 0.4$ on shells of redshift, and as projected onto the Supergalactic plane in Figure 11. Note that the Mark III galaxies have an *IRAS* predicted mean Hubble flow of 2.9%, which was removed in the process of smoothing the *IRAS* predicted field by the mode expansion. Residual fields are shown in Figures 12-14 for $\beta = 0.4$ and 0.7. Note the similarities and differences between these Figures and Figures 5-6 for the mock catalog. It is important to remember that the ITF velocity and *IRAS* gravity fields have been processed completely independently of each other. To a first approximation, the agreement between these Figures is a spectacular and remarkable confirmation of the consistency between the gravity and velocity fields of our local Universe. The *IRAS* galaxies must have some close relationship to the underlying mass distribution. The qualitative alignment of the fields is consistent with the large scale structure having been formed by the process of gravitational instability.

On the other hand, the residual fields, for any value of β , are not nearly as clean as seen in the mock catalogs, and are always dominated by strong dipole patterns that increase linearly with redshift. This is especially pronounced for the higher values of β and is particularly clear in Figure 14. The *IRAS* maps never reproduce the strong shear seen in the ITF maps between the Hydra and Centaurus regions. They never reproduce the strong infall measured by ITF for the $l = 180^\circ$, $b = 45^\circ$, $cz = 5000 \text{ km s}^{-1}$ region. For $\beta \leq 0.3$ (not shown), the local supercluster flow is much too small, and the flow toward Perseus-Pisces is too small. For $\beta = 0.4$, the residual field in the local zone is still completely coherent, but the flow toward Perseus-Pisces and the average of Hydra and Centaurus is approximately correct. For $\beta = 0.7$ the relative motion toward Virgo matches the ITF measurement (-340 km s^{-1} in the LG frame) but the flow away from Perseus-Pisces and toward the Great Attractor complex is now too large.

4.3 The Dipole Residual on Shells

The residual field between the ITF and *IRAS* fields is clearly dominated by the dipole component. ND94 emphasize that the dipole component of the radial peculiar velocity field on a shell, relative to the LG, is generated entirely by the mass distribution within that shell; the exterior mass distribution affects only quadrupole and higher l perturbations.

Thus it is critical to seek agreement of the dipole components of the fields on modest scales, $cz < 6000 \text{ km s}^{-1}$, where the data are best.

Although the large spatial inhomogeneity of the Mark III data strongly mixes the modes together, it is possible to extract the dipole component of the field. Consider binning the Mark III data into shells of redshift 1000 km s^{-1} thick. Then compute the three components of a dipole v_D by summing the radial peculiar velocity v_j over the j galaxies in the shell:

$$v_D = \frac{\sum_j v_j w_j \cos(\theta)}{\sum_j w_j \cos^2(\theta)}, \quad (19)$$

where θ is the angle from the three unit vectors $\hat{\mathbf{x}}, \hat{\mathbf{y}}, \hat{\mathbf{z}}$. By using a weight function w_j given by $(\delta\theta_4)^{-2}$, where $\delta\theta_4$ is the angle of galaxy j to its fourth nearest neighbor on the given shell, the computation of v_D is approximately equal area weighted, as is appropriate for comparison to the original functional expansion.

An example is shown in Figure 15, where we plot the ITF and *IRAS* (for $\beta = 0.6$) derived dipoles in six shells within 6000 km s^{-1} . The open and closed symbols are derived from the irregularly spaced Mark III galaxies, while the solid lines are original *IRAS* dipole components, for $\beta = 0.6$, based on the full 1.2 Jy sample. Note that the *IRAS* derived points, drawn from a less than optimal sky distribution, still match the smooth curve very well, demonstrating that recovery of the dipole from the irregularly spaced Mark III sample is not a problem. The open squares showing the ITF dipole are consistent with the *IRAS* dipole in the Z component, and the total amplitude is a good match as well. But the X and Y components are seriously discrepant. The X component is consistent for the first three shells, but then deviates substantially, while the Y component is discrepant for all shells; *IRAS* predicts a substantial reflex dipole in the Y component that should grow with redshift, but little is detected in the ITF data. For those who have followed this subject for some time, this discrepancy is not new (see e.g. the comparison of Faber and Burstein (1988) with the discussion by Strauss and Davis (1988) and Yahil (1988)). The *IRAS* field expects to find substantial “backside infall” at the Centaurus region and beyond, but such a signature is very weak in the Mark III data. We emphasize once again that the comparison under consideration here is for spiral galaxies only; the discrepancy is observed for both spiral and elliptical galaxies.

5. Likelihood Analysis of Modal Comparison

5.1 The scatter of ITF and *IRAS* coefficients

Given the measurement of the coefficients α^j derived from the Mark III and *IRAS* fields, how can we best compare them? In the discussion above, we compared the fields galaxy by galaxy, and by means of the area weighted dipole on shells. The sky maps are appropriate for visualization; however the fields as seen in space are highly correlated because of the strong covariance of the errors in the ITF velocities as well as in the *IRAS* gravity. Since the number of modes which describe the fields is significantly less than the number of galaxies in the Tully-Fisher sample, a galaxy by galaxy comparison requires inversion of an unduly large covariance matrix. Therefore we work directly with the recovered mode coefficients

from the ITF and the *IRAS* gravity in order to assess the quantitative agreement between the velocity and gravity fields.

Figure 16 plots the coefficients α_{tf} versus α_{iras} for the real data, using $\beta = 0.6$ for the *IRAS* coefficients. Also shown are the coefficients for one realization of the mock catalog; in this case we can also plot the coefficients α_{tf} versus α_{true} . Note in the mock case that the coefficients track the diagonal line extremely well, consistent with $\beta = 1$. As expected, the noise is increased for the ITF versus *IRAS* comparison. Different realizations of the mock catalog all have consistent behavior in their mode-mode scatter diagrams.

5.2 The error matrix on ITF and IRAS coefficients

As is shown in ND, the orthonormality condition leads to the following simple form for the error matrix of the ITF coefficients, namely,

$$\langle \delta\alpha_{tf}^j \delta\alpha_{tf}^{j'} \rangle = \left(\frac{\sigma_\eta}{s} \right)^2 \delta_{jj'}^K. \quad (20)$$

In Figure (16), the plot of α_{tf} versus α_{true} for the mock catalog has noise that is completely consistent with equation (20), as expected.

For the Mark III catalog, six separate samples, with differing photometric bandpasses and velocity width methods, have been pieced together in the manner described above. The offsets in the magnitudes and linewidths for this adjustment have uncertainty in the mean, and this will translate into a non-diagonal contribution to the covariance matrix $\langle \delta\alpha_{tf}^j \delta\alpha_{tf}^{j'} \rangle$. We estimated this contribution by generating 20 realizations of the Mark III catalog with gaussian errors in the zero point of the different pieces appropriate for each subsection. We then directly estimated the covariance matrix generated by these offsets, and included them in the analysis below. In fact, the errors in the zero points are small and make no difference to the error budget.

The situation for the modes of the *IRAS* predicted velocity field is not so simple, however. The error matrix $\langle \delta\alpha_{iras}^j \delta\alpha_{iras}^{j'} \rangle$ has to be constructed from the covariance matrix of the *IRAS* predicted velocities of galaxies. Using Equation (15), and linearizing the errors in the velocities about the predicted values yields,

$$M^{jj'} \equiv \langle \delta\alpha_{iras}^j \delta\alpha_{iras}^{j'} \rangle = \left(\frac{5}{2.3} \right)^2 \sum_{ii'} \frac{\langle \delta u_i \delta u_{i'} \rangle}{z_i z_{i'}} \frac{1}{(1 - (u_i/z_i))} \frac{1}{(1 - (u_{i'}/z_{i'}))} \tilde{F}_i^j \tilde{F}_{i'}^{j'} \quad (21)$$

where $\langle \delta u_i \delta u_{i'} \rangle$ is the covariance matrix of the *IRAS* predicted velocities of galaxies j and j' after subtracting the Hubble-like flow as described in 2.2.2. Note that even if this velocity covariance matrix is diagonal with equal elements, the covariance matrix of the coefficients will not be diagonal, as the modes \tilde{F} are orthogonal with unit weighting of each point, whereas the sum above is weighted approximately as z_i^{-2} .

The *IRAS* velocity field is a very nonlocal quantity, effectively computed by counting the vector sum of all *IRAS* galaxies around a given point, weighted by the inverse of the square of the real space separation and by the inverse of the selection function. This

sum is computed over a discrete set of points in a finite catalog, and therefore must suffer from Poisson noise and from variance induced by the assumption that the mass per *IRAS* galaxy is assumed constant for each redshift shell (c.f. Strauss *et al.* 1992). In addition, the computed velocities assume linear theory, yet there exist high density zones within the galaxy distribution for which linear theory is known to be inaccurate and for which the deviations are likely to be coherent (as in triple-valued zones or zones which have shell crossed). There are incoherent small-scale nonlinear velocities unresolved by the *IRAS* procedure which add noise as well. Furthermore, the *IRAS* predicted velocities are sensitive to the assumed transformation from heliocentric to LG frame velocities, which might be in error by perhaps 50-100 km s⁻¹. All of these error sources contribute to errors in the *IRAS* reconstructed velocities, and most of these errors are coherent.

We can express the *IRAS* velocity covariance as a sum over these terms, writing

$$\langle \delta u_i \delta u_j \rangle = C_{SN}(i, j) + C_{NL}(i, j) + \sigma_{LG}^2 \cos(\theta_{ij}) \quad (22)$$

where $C_{SN}(i, j)$ is the covariance in the predicted peculiar velocities due to the Poisson noise, C_{NL} is a term to describe the deviations from linear theory, and σ_{LG} is the uncertainty in the transformation to LG frame. We shall set $\sigma_{LG} = 100$ km s⁻¹. Note that this term alone generates complete covariance of all *IRAS* predicted peculiar velocities.

The Poisson noise term $C_{SN}(i, j)$ can easily be derived from a distribution of points in *real* space (Yahil *et al.* 1991) where, according to linear theory, the peculiar velocity field is related to the distribution of galaxies by the Poisson equation, and the variance C_{SN} would scale as β^2 . However, the galaxies are observed in redshift space and the error in the predicted velocity field must be computed according to the relation (4), for which the scaling with β is not trivial. An analytical expression for C_{SN} for the velocities from (4) is cumbersome and numerically expensive to evaluate. Thus we choose to compute the covariance matrix C_{SN} by generating 18 bootstrap realizations of the observed 1.2 Jy *IRAS* galaxy distribution by replacing each observed galaxy with a number of points drawn from a Poisson distribution with mean of unity. Then we compute the velocity fields from these realizations by the same algorithm used in the derivation of the velocity field from the observed galaxy distribution. For galaxy i of the Mark III sample, we tabulate the differences, δu_i , between the velocity obtained from each of 18 bootstrap realizations and the velocity as predicted from the actual distribution of galaxies, and evaluate the covariance matrix C_{SN} by averaging the product $\delta u_i \delta u_j$ from all the bootstrap realizations. This process is computed for several different values of β .

The term $C_{NL}(i, j)$ describing nonlinear effects can be modelled as

$$C_{NL}(i, j) = \sigma_u^2 \delta_K^{ij} + ((s_h(i) + s_h(j))^2 \exp\left(-\frac{|\mathbf{r}_i - \mathbf{r}_j|^2}{2\sigma_{coh}^2}\right)), \quad (23)$$

where particles have an assumed incoherent small scale 1-D velocity dispersion σ_u , but in regions of high shear can also display coherent errors, with coherence length σ_{coh} which we set equal to 300 km s⁻¹. Miller *et al.* (1996) have directly measured σ_u for the *IRAS* 1.2 Jy survey, and derive a best value $\sigma_u = 137$ km s⁻¹. Willick *et al.* (1996c) find a best value

of $\sigma_u \approx 150 \text{ km s}^{-1}$ for the Mark III galaxies using the VELMOD analysis (i.e. “Method II+” as described by Strauss and Willick (1995)). The Mark III and *IRAS* galaxies need not have the same thermal dispersion, but the agreement is comforting. We shall assume a value $\sigma_u = 150 \text{ km s}^{-1}$. The coherent error we assume is proportional to the square of the average shear in the *IRAS* derived velocity field, $s_h(i) \equiv 100 \min(1, |dv_p/dz|) \text{ km s}^{-1}$, which is an approximately linear function of β . This term is designed to deweight points in regions of probable shell crossing, where the *IRAS* predicted shear is large.

5.3 Pseudo χ^2 analysis

Our basic assumption is that, for the true β , the ITF and the *IRAS* velocity fields are noisy realizations of the true underlying velocity field. Let α^j be the coefficients obtained from the modal expansion of the true underlying field. Each estimated coefficient is derived from a sum over a large set of numbers, so by the central limit theorem we expect each estimated coefficient to have a normal distribution, even if the underlying velocity field or Tully-Fisher data has nongaussian scatter. Since the Mark III and the *IRAS* data are independent we write the probability for measuring α_{iras}^j and α_{tf}^j as,

$$P[\alpha_{iras}^j, \alpha_{tf}^j | \alpha^j] = A \exp\left[-\frac{1}{2}(\chi_{tf}^2 + \chi_{iras}^2)\right] \quad (24)$$

where we have defined,

$$\chi_{tf}^2 = \sum_j \frac{(\alpha^j - \alpha_{tf}^j)^2}{\sigma_{tf}^2}$$

and,

$$\chi_{iras}^2 = \sum_{j,j'} (\alpha^j - \alpha_{iras}^j)(M_{jj'}^{-1})(\alpha^{j'} - \alpha_{iras}^{j'}).$$

Note that χ_{tf}^2 does not depend on β . Given β , we seek the true coefficients, α^j , and β , by maximizing the probability (24). Therefore our best estimates are obtained by solving,

$$\partial P / \partial \alpha^j = 0, \quad (25)$$

and,

$$\partial P / \partial \beta = 0. \quad (26)$$

Since the normalization of the probability (24) does not depend on the coefficients α^j , the condition (25) implies that the parameters α^j which maximize P for a given β renders a minimum in the total $\chi^2 \equiv \chi_{iras}^2 + \chi_{tf}^2$. However, since the error matrix M and hence the normalization factor A strongly depend on β , the maximum of P with respect to β does not necessary coincide with the minimum of χ^2 . Though, at a given β , the condition (25) yields a set of linear equations for α^j which can be solved using standard methods, the condition (26) leads, in general, to a complicated nonlinear algebraic equation for β . Therefore, a simultaneous estimation of the coefficients α^j and β is a problem of nonlinear

minimization. Fortunately, in this particular case, it is easy to see that solving (25) and (26) simultaneously can be achieved by the following scheme: solve (25) for α^j at a given β and compute the corresponding value of $P(\beta)$. The estimate for the true β is the value which renders $P(\beta)$ a maximum. The condition (25) yields,

$$\boldsymbol{\alpha} \cdot \left(\mathbf{I}\sigma_{tf}^{-2} + \mathbf{M}^{-1} \right) = \boldsymbol{\alpha}_{tf} \cdot \mathbf{I}\sigma_{tf}^{-2} + \boldsymbol{\alpha}_{iras} \cdot \mathbf{M}^{-1}. \quad (27)$$

By substituting (27) for α^j in the total χ^2 , we have,

$$\chi^2|_{\partial\chi^2/\partial\alpha^j=0} \Rightarrow \chi_{tf}^2 + \chi_{iras}^2 = \sum_{j,j'} \left(\alpha_{tf}^j - \alpha_{iras}^j \right) \left(\mathbf{I}\sigma_{tf}^2 + \mathbf{M} \right)_{jj'}^{-1} \left(\alpha_{tf}^{j'} - \alpha_{iras}^{j'} \right), \quad (28)$$

which reduces to the pseudo χ^2 suggested by Press *et al.* (1992) for problems with errors in both the x and y directions. Note that the difference between the values of β which minimize the $\chi^2(\beta)$ and maximize the probability $P(\beta)$ must be consistent with the errors in their estimates provided that the ITF and *IRAS* coefficients differ only because of the noise in their measurements.

Comparing the Tully-Fisher coefficients α_{tf}^j to *IRAS* derived coefficients α_{iras}^j for the mock catalog gives $\chi^2 = 53.5$ for 56 degrees of freedom. Thus the fit of the coefficients of the mock catalogs is entirely consistent with the expected noise, and this consistency is seen in all the realizations of the mock catalog. When we apply equation (22) to the mock catalog, comparing the Tully Fisher coefficients α_{tf}^j to the *true* coefficients α_{true}^j , while holding M_{ij} nonzero, we obtain $\chi^2 = 30.2$ for 56 degrees of freedom. This low χ^2 results from inappropriate inclusion of the *IRAS* like covariance; the approximate halving of the χ^2 demonstrates that the errors introduced by the imprecision of the *IRAS* estimates are similar in magnitude to those of the ITF estimate.

The results of applying this same procedure to the real data is given in Table 1, where we list χ^2 versus β . For each value of β we first computed $M^{jj'}$ (equation 16) and then evaluated equation (23). The table shows that the minimum $\chi^2 = 100$ (55 d.o.f.) at $\beta = 0.5$. Given that χ^2 for ν degrees of freedom has an expected mean of ν and a variance of 2ν , the best χ^2 is 4.3σ deviant from its expected value. The fit is statistically very improbable and can be rejected. That is, although the mock catalogs demonstrate that the procedure is capable of producing very acceptable χ^2 results, the actual comparison of Mark III to *IRAS* leads to the conclusion that the fields are statistically inconsistent with each other. The details of the best β and the level of inconsistency are weak functions of how the catalogs are limited; we would derive a higher β if we limited the catalogs to $cz < 4000 \text{ km s}^{-1}$, but the fit would remain unacceptable.

Because the residual field is dominated by a strong dipole and because we believe we understand the error matrix, it is not permissible to simply double the covariance matrix to bring the χ^2 values to reasonable levels. Thus we urge extreme caution in concluding that $\beta = 0.5 \pm 0.1$ is in any sense a “best fit” solution.

6. Discussion

6.1 Alternative Methods and Results

The ITF analysis is only one of several, independent methods of comparing the Tully-Fisher catalogs with the redshift survey catalogs. Given the difficulty of the comparison and the subtlety of the error analysis, it is worthwhile to investigate alternative approaches and to expect consistent results. Only then will we have confidence in the derived value of β .

The great advantage of the ITF scheme is that it allows the comparison of the velocity and gravity field mode by mode, with identical resolution to each field. The Monte-Carlo simulations with realistic mock catalogs confirm that the bias in the extracted velocity field is negligible. The method allows for the gradient in radial resolution of the two fields, so it is capable of extracting the maximum useful information for each field. One can rank order the modes by their significance, or contribution to χ^2 , keeping only the most significant modes, so as to provide a very compact description of the field. This is an example of a Karhunen-Loève transformation (Therrien 1992). Recent applications of this technique to astrophysics include the CMBR fluctuations of the COBE data (Gorski 1994, Bunn 1995, Bond 1995), the power spectral analysis of fluctuations in redshift surveys (Vogeley and Szalay 1996), and the spectral classification of galaxies (Connolly *et al.* 1995).

The “VELMOD” approach of Willick *et al.* (1996c; cf. the preliminary discussion presented by Strauss & Willick 1995, § 8.1.3) is in several respects complementary to the analysis presented here. VELMOD also makes a comparison of the Mark III TF data and the gravity field derived from the *IRAS* 1.2Jy redshift survey. It differs from the ITF analysis in explicitly accounting for the small-scale velocity dispersion σ_u , which it treats as a free parameter, and in allowing for the possibility of multivalued redshift-distance diagrams; the ITF reconstruction implicitly assumes a unique redshift-distance mapping. Implementation of VELMOD is done using grid-based, real-space *IRAS* velocity reconstructions, as opposed to the noniterative redshift-space *IRAS* velocity fields used here. Thus, VELMOD and ITF do not use identical gravity fields, although tests have shown them to be very similar.

There are several advantages to VELMOD. First, in accounting for small-scale velocities and arbitrary redshift-distance diagrams, it determines the probabilities of individual data points without some of the approximations used here, and thus provides a reliable maximum likelihood statistic. It does not require that the input TF catalog be placed on a common system, but instead treats the individual sample TF relations as free parameters. This makes it free of the uncertainties induced by the overlap-comparison procedure described above (§ 4.1). Finally, VELMOD is particularly well-suited to analysis of the nonlinear regime, which holds the promise of breaking the Ω - b degeneracy. However, VELMOD has an important weakness from which neither ITF nor POTENT suffers: it does not permit the construction of a velocity field from the TF data alone; instead, it assumes that the *IRAS* velocity field, for some value of β (and b), is a good fit to the data, and selects the best β by maximizing likelihood. Yet as we have shown in this paper, the *IRAS* velocity field does not fit the data well throughout the sampled volume. In such a circumstance, the meaning of the maximum likelihood statistic is unclear. In addition,

VELMOD is not well suited to a proper analysis of covariant velocity field prediction errors, such as we have carried out here.

A final distinction derives from the depth of the respective analyses. VELMOD is rather cpu-intensive and, moreover, differs meaningfully from analyses such as ITF only when σ_u is a substantial fraction of the TF distance error. The analysis of Willick *et al.* (1996c) is thus restricted to redshifts $cz \leq 3000 \text{ km s}^{-1}$. In contrast, we have extended our computationally more efficient analysis to twice that distance. As noted above, our low indicated value of $\beta = 0.4 - 0.6$ is in part a consequence of discrepancies between the ITF velocity field and the *IRAS* gravity field that are manifest principally at distances $\gtrsim 4000 \text{ km s}^{-1}$. Willick *et al.* (1996c) analyze their likelihood fit residuals and find them to be nearly incoherent across the sky, which reflects the fairly good agreement between *IRAS* and the TF data within $\sim 3000 \text{ km s}^{-1}$. Preliminary results seem consistent with our “best” values of β .

Both the POTENT and ITF methods have been validated by extensive testing with mock catalogs, so it seems reasonable that they should yield consistent results. We here list several relative advantages and disadvantages between the ITF method and the POTENT/*IRAS* comparison.

- (1) POTENT provides a measure of the divergence of the velocity field which can be compared to the directly observed galaxy density field. Both fields are local, an obvious advantage. The ITF field must be compared to the non-local *IRAS* derived velocity field. These fields are both susceptible to systematic errors within the data.
- (2) POTENT required a large, uniform smoothing to properly define the smoothed velocity and velocity potential. Dekel *et al.* (1993) have been using a gaussian smoothing of width $\sigma = 1200 \text{ km s}^{-1}$, sufficient to filter out the infall of the Local Group toward the Virgo cluster. The ITF method can work with much smaller smoothing, and the smoothing length can be dependent on redshift. This is quite advantageous, since the statistical precision of both the velocity and gravity field are decreasing functions of distance. On the other hand, the ITF method can readily accomodate uniform smoothing, if that is desired.
- (3) The POTENT analysis is dependent on a calibrated forward Tully-Fisher relation (i.e. $M = M(\eta)$, where M is the absolute magnitude and $\eta \equiv \log(\Delta v)$ is the velocity width parameter), and the analysis is sensitive to Malmquist bias (see Strauss and Willick 1995 for details). The ITF analysis uses an *inverse* TF relation (i.e. $\eta = \eta(M)$); the parameters of this relation can be fitted at the same time as the mode coefficients. As long as the galaxy selection is independent of linewidth, this method does not suffer from Malmquist bias. The ITF method is biased in the presence of a thermally hot velocity field, where multistreaming is very pronounced; however, given the estimated amplitude of the small scale peculiar velocity field of galaxies, this bias is quite modest, as described above (see ND95 for details).
- (4) The ITF method is simply a redshift space smoothing algorithm for the Tully-Fisher data that enables one to get a measure of the velocity field without binning the

data. It is not intended for the construction of full-sky velocity maps, and such maps are not needed for comparison to the gravity field. The method compares the two fields only where there are data. By avoiding binning of the data, it eliminates the “sampling gradient bias” that is a serious problem for POTENT. Both the ITF and *IRAS* analyses are here carried out in observed redshift space, whereas most previous analyses, including POTENT, have been done in real space. Since the inversion to real space is not unique in the multi-valued zones, attempting to perform the ITF analysis in real space would present additional very serious complications. However, with sufficiently precise distance indicators, working in redshift space will not take full advantage of the data, since multivalued zones could be resolved (e.g. Strauss and Willick 1995).

- (5) By filtering the density and velocity fields with identical functions, one can be confident the fields have identical resolution. In the POTENT analysis, assessing the relative resolution of the galaxy density field compared to the inferred mass density field is not straightforward. Previous velocity-velocity comparisons have been especially compromised by the inability to filter the velocity field. Although we have here chosen a very general set of functions for the mode expansion, if desired, it would be straightforward to supplement this expansion with additional functions to describe known features, such as Virgocentric infall. This would be an appropriate route for datasets smaller or more concentrated in selected directions than Mark III.
- (6) The full covariance matrix of the coefficients of the ITF and *IRAS* fields can be computed, and because the matrix is modest in size, it can be readily inverted. This is essential for a proper statistical assessment of the fit. POTENT compares velocity/density fields computed on a grid, and the error in β must be estimated using sophisticated Monte Carlo methods. All previous point by point velocity-velocity comparisons have failed to include this essential covariance in the error matrix of the gravity field.

6.2: Why Don't the Fields Agree?

The ITF method has led to an unambiguous measure of the Tully-Fisher velocity field, one we feel is correct within the limited resolution of our chosen expansion. The biases generated by small-scale thermal velocities are modest. There is undoubtedly additional information that could be gleaned from the Mark III database, as our basis function of modes is not necessarily optimal for the derivation of the divergence of the flows, the critical information extracted in the POTENT analysis. The tests with the mock catalog validate our approach, and demonstrate that comparison of the Mark III data with the *IRAS* derived field should yield consistent fields. The error matrix of both the Mark III and *IRAS* derived mode coefficients is, we believe, well understood. Yet the comparison of the modes conclusively demonstrates that they are not consistent within their errors at the $4\text{-}\sigma$ level. We have already used a very generous Tully-Fisher error, $\sigma_\eta = 0.05$ (corresponding to $\sigma_M \approx 0.45$). Increasing this error will reduce the formal χ^2 but will not remove the coherent residuals.

The nature of the inconsistency is dependent on the depth of the sample under consideration. To fit the Local Supercluster will require $\beta \gtrsim 0.7$, but the large dipole residual at large scales demands a smaller β . Thus it is not surprising that the “best” β for our analysis, $\beta = 0.4 - 6$, is slightly lower than suggested by VELMOD , $\beta = 0.57$, as that analysis is confined to galaxies with $cz < 3000 \text{ km s}^{-1}$.

The $4\text{-}\sigma$ discrepancy between the *IRAS* derived velocity field and the Mark III velocity field suggests that the problem is not due to random errors in either field, but to systematic problems in one or both datasets. There are many possible sources of systematic errors, and we here list and discuss the most obvious among them. It is very likely that some combination of these errors is responsible for the statistically poor correspondence of the fields, and until we can deal with the major problems, all derivations of β from flow analysis must be considered suspect.

- (1.) *The IRAS field is missing the early type galaxies, so it ignores cluster centers.* Careful comparison of the counts of *IRAS* galaxies to optically selected galaxies indeed shows an underrepresentation of the galaxies within the centers of clusters (e.g. Virgo’s core is underrepresented by a factor of 2). However the cores of clusters do not dominate the mass of the superclusters (recall that the cluster mass typically diverges as radius R), and the *IRAS* galaxies appear to be good tracers of the general field population (Strauss *et al.* 1992). “Boosting” known cluster centers to compensate for the missing early type galaxies does not lead to a better fit between the gravity and velocity fields, but it will reduce the best estimate of β by a factor of ≈ 1.3 .
- (2.) *The IRAS field does not have whole sky coverage and is missing a prominent cluster in the Zone of Avoidance.* Recently Kraan-Korteweg *et al.* (1996) have reported on a Coma-like cluster, A3627, with estimated mass $2.5 \times 10^{15} h^{-1} M_{\odot}$ at position $l=325^{\circ}$, $b=-7^{\circ}$, $cz_{LG} \approx 4700 \text{ km s}^{-1}$. Although the *IRAS* survey does include galaxies to $|b| > 5^{\circ}$, and the observed galaxy density is interpolated through the Galactic plane, a cluster of entirely early type galaxies would have been severely undercounted. The *IRAS* catalog has an overdensity of galaxies at the position of A3627, but it is not sufficient to comprise a large Coma-like cluster, and it is not by any means the most massive *IRAS* cluster in this vicinity. Could this possibly explain the strong shear observed in the ITF analysis between the Hydra and Centaurus regions? Suppose that the *IRAS* survey has given no mass to A3627. Then for the parameters above, the neglect of A3627 has led to an error of the peculiar motion of the LG of $\approx 50\Omega^{-0.4} \text{ km s}^{-1}$. We can readily compute the missing differential motion between the Centaurus clusters at $(l,b) = (302^{\circ}, 22^{\circ})$ and the LG caused by A3627. If Centaurus is at distance of $\approx 3800 \text{ km s}^{-1}$, as suggested by the *IRAS* field, then its acceleration toward A3627 is in the transverse direction. If the distance of the Centaurus clusters is lowered to 2500 km s^{-1} , as suggested by several distance estimates (Lynden-Bell *et al.* 1988; Dressler 1994), then the differential radial acceleration between Centaurus and the LG induced by A3627 is only $4\Omega^{-0.4} \text{ km s}^{-1}$. The differential influence of A3627 on Hydra (at $(l, b, cz) = (275^{\circ}, 20^{\circ}, 4500 \text{ km/s})$) and the LG is approximately $75\Omega^{-0.4} \text{ km s}^{-1}$. These results scale linearly with the mass of A3627. Thus as one increases the mass of A3627, the residuals toward Hydra become more negative whereas the residuals

toward Centaurus are changed by a negligible amount. This is the wrong sense, since the residuals toward Centaurus are far worse than those toward Hydra. Furthermore, the effect of a missing cluster like A3627 is modest compared to the residuals to be explained. Examination of the *IRAS* density field at this redshift demonstrates that the total mass overdensity in the Hydra-Centaurus-Pavo-Indus complex greatly exceeds that of any missing cluster center, and that the addition of the core of A3627 makes no difference to the overall density field.

- (3.) *The IRAS field has poor convergence to the CMB dipole either because of dilute sampling noise at large distance or because of an improper transformation to the Local Group frame.* The ITF method is sensitive to the choice of the LG frame. The Mark III data, when analysed by the POTENT algorithm, exhibits a bulk motion of 250–300 km s⁻¹ that is not observed in the *IRAS* derived gravity field (Dekel 1995). If this is due to an incorrect choice of the LG frame, then the effect is in the direction of the nearby Maffei/Dwingeloo group of galaxies (Kraan-Korteweg *et al.* 1994), which are highly obscured and are not included in the *IRAS* gravity field. If they are the source of this anomalous motion, then they should be blueshifted by our infall toward them. However they are observed to have redshifts, not blueshifts, and so must move coherently with the Milky Way. Beyond the local galaxies in this direction is a void, which should repel us, not attract us. It is difficult to understand how the LG could have a local source of acceleration leading to a velocity as large as that induced by the Virgo supercluster, without leaving any signature in the local galaxy distribution. The local flow field has only modest shear, and a large error in the LG frame definition is unlikely. This is apparent in Figures 8, 14, and 15; for shells within 2000 km s⁻¹, the dipole residual between the ITF and *IRAS* fields is very modest. An error in the LG frame would lead to dipole residuals *constant* with redshift, whereas the observed dipole residual grows approximately linearly with distance (Figures 14 and 15). The local flow is rather quiet (Peebles 1992; Schlegel *et al.* 1994) and shows no evidence of the very large local shear that would result if the LG frame were offset by several hundred km s⁻¹.

As a test of the redefinition of the LG, we have generated *IRAS* fields and ITF fields with the LG frame offset toward Maffei by 200 km s⁻¹. Such an offset leads to smaller residuals toward Perseus-Pisces for high values of β , compared to Figure 14, but instead there are coherent errors toward Hydra and other nearby regions, as expected. We were unable to achieve a better fit by adjusting the LG frame.

The diluteness of the *IRAS* density field could lead to substantial errors in the predicted u_{iras} field, especially from matter at redshifts $cz > 6000$ km s⁻¹ (Davis *et al.* 1991). The mock catalogs demonstrate the degree of expected error. However, errors in the density field of external matter will not affect the $l = 1$ residuals in the LG frame. These dipole residuals, if real, are indicative of a mass field not traced by the *IRAS* galaxies. Since we expect linear theory to apply, we can simply estimate the unseen mass density by taking the divergence of the residual dipole field. Making allowance for the transverse fields by assuming potential flow, and noting that the residual field scales approximately linearly with redshift, we find a residual mass field

$\delta_\rho \propto \cos\theta$, where θ is the angle from the apex direction. This is a very strange density field, one that is constant in redshift but tilted toward a particular direction. Thus the residual dipole field cannot be considered physically reasonable; it must be indicative of some systematic discrepancy.

The reason our results are not consistent with the high β values derived from the density/density comparisons (Dekel *et al.* 1993) using the POTENT algorithm is clear from Figure 14. For large values of β the dipole residual growing linearly with z is very pronounced. It cannot be removed by a transformation of the LG center, nor can it be explained by an external mass field. It can only be reduced by elimination of some unknown systematic error in one of the catalogs, or the reduction of β . The POTENT algorithm, by taking the derivatives of the Mark III velocity field, is less sensitive to this large scale dipole, but it is more sensitive to higher spatial frequency components of the flow field. This very different weighting of the data, combined with the poor quality of the fit of *IRAS* to Mark III for any value of β , is sufficient to explain why it is not unreasonable for the ITF/VELMOD algorithms to yield “best” β values that are inconsistent with the best estimates derived from POTENT using the same data. One could argue that the difference in the derived values of β is the result of a strong scale dependence of the biasing relation. However, as shown by Kauffman, Nusser and Steinmetz (1996), all physically reasonable bias mechanisms for hierarchical models of structure formation are well approximated as linear, scale independent biasing for scales larger than a few Mpc.

- (4.) *The Mark III database is not truly uniform; the effort to unify the five individual sections of Mark III to a common linewidth, magnitude system is somehow deficient.* The Mark III sample is a collection of available data and samples different directions far from uniformly. There is a large concentration of galaxies toward Perseus-Pisces contributed by Willick (1990), and a very large concentration of galaxies in the Southern sky contributed by Mathewson *et al.* (1992) on the opposite side of the sky. More importantly, different techniques are used in different directions. Any inconsistencies within the Mark III catalog are likely to translate into dipole effects, and indeed the dominant residuals between Mark III and *IRAS* is a dipole aligned along the center of the MAT subsample.

Willick *et al.* (1996a,b) describe the comparison of the different pieces of the Mark III sample. It is obviously critically important to insure that the relative photometry and linewidth measurements are standardized, and it is possible that the Mark III data has zero point calibration problems between its different subpieces. As described above, we have tested the sensitivity of the ITF field to the known statistical uncertainty of the zero-point offsets, finding a negligible effect. If calibration mismatches are the source of the problem, then the error must be considerably in excess of the measured statistical errors. It would be especially valuable to obtain additional data to better tie together the different pieces of Mark III, and to improve the sky coverage in the North and away from the dense cluster centers. The Mark III sample is vulnerable to any systematic nonuniformities between Han-Mould Northern versus Southern clusters, because this subsample is used to renormalize the different pieces of Mark III to one system. A new

survey of Tully-Fisher distances for 300 galaxies in the zone $5000 < cz < 7000 \text{ km s}^{-1}$ around the entire sky is just now getting under way (Strauss *et al.* 1996), with the goal of better calibration of the whole-sky samples.

A considerable portion of the Mark III sample is derived from relatively low galactic latitude data, where corrections for galactic extinction are significant. Recently Schlegel, Finkbeiner, and Davis (1996) have been studying whether a new extinction map, based on the COBE/DIRBE data, leads to significantly different flow fields. The question is still under investigation, but the answer appears to be no.

- (5.) *The Tully-Fisher calibration is dependent on environment and the residual field is caused by changes in the TF parameters for different sections of the sky.* Although it is impossible to prove that the TF relation is independent of environment, it is not easy to imagine schemes whereby the relation is coherently different in one portion of the sky compared to another. It is much easier to imagine environmental dependence leading to larger scatter of the TF relation. It is important to note that the most serious zone of discrepancy, in the Centaurus region, has been extensively studied with the $D_n - \sigma$ relation for ellipticals (Lynden-Bell *et al.* 1988) as well as recent surface brightness fluctuation measurements using ellipticals (Dressler 1994; Tonry and Dressler 1995). All three distance indicators suggest strong outflow in the Centaurus region, which the *IRAS* maps fail to predict.

Improving the *IRAS* maps by going to denser sampling, either using the PSC catalog (Saunders *et al.* 1995), or by supplementing the *IRAS* catalog with optical data in regions not too badly extinguished (e.g. Santiago *et al.* 1995), will be an important next step to attempt to resolve the discrepancies here presented. Based on previous analyses (Hudson 1994; Freudling & da Costa 1994), these improvements in the gravity map are unlikely to resolve the problem. More uniform full-sky Tully-Fisher catalogs, where the line widths and magnitudes are estimated in a consistent fashion for the entire sample, will be an enormous step forward, but this is a major undertaking.

7. Summary

We have presented a method for comparing the velocity field derived from Tully-Fisher type data with the gravity field derived from full-sky redshift surveys of galaxies, such as the *IRAS* surveys. The chief strength of the method is that the two fields are filtered through the same set of low resolution modes, so that one is assured they indeed have the same resolution. In spite of working in the ‘inverse’ direction, we are able to produce pictures of the measured fields.

Although the method works extremely well in mock catalogs, with modal coefficients fully consistent with the expected noise, we find a much poorer agreement for the real data. This discrepancy is not consistent with random errors, and may be indicative of a systematic error in one or both of the datasets. We derive a “best” value of $\beta = 0.4 - 0.6$, in reasonable agreement with the value derived from the VELMOD analysis, though considerably smaller than the values ($\beta \simeq 1.0$) typically obtained from applications of the POTENT algorithm. Because the χ^2 for the fit of the ITF velocity field to the

IRAS gravity field is 100 for 55 degrees of freedom, the fields cannot be said to agree in detail. We therefore urge extreme caution in concluding that β has been measured in large scale flows. It is worth emphasizing that there is qualitative agreement between the velocity and gravity fields, particularly at distances $\lesssim 3000 \text{ km s}^{-1}$. However, until the discrepancies on larger scales can be resolved, and all methods give consistent answers, we must prudently consider the value of β to be an open question.

Future work should greatly improve this situation, as more data, and more precise data, become available. The Mark III catalog is not optimal for the analysis presented here, since the sky coverage is relatively nonuniform. For a given allocation of telescope time, the optimal strategy is to sample the sky to a given depth as uniformly as possible. Full sky samples are difficult to calibrate in a uniform manner, but are worth the effort, since they provide the only route to estimation of the low order multipoles of the local velocity field.

Acknowledgments

This work was supported in part by NSF grant AST 92-21540 and NASA grant NAG 51360. AN acknowledges the support of a PPARC postdoctoral fellowship. We thank Simon White for the use of the large N -body simulation and we acknowledge helpful discussions with Saleem Zaroubi. JAW would like to acknowledge the contributions of his collaborators on the Mark III project, Avishai Dekel, Sandra Faber, David Burstein, and Stéphane Courteau. We thank Michael Strauss and the referee Michael Vogeley for numerous helpful comments that have substantially improved the manuscript.

Table 1: Coefficient Comparison

β	χ^2
0.1	155
0.2	124
0.3	107.5
0.4	100.5
0.5	100
0.6	102.8
0.7	112
0.8	121
0.9	134
1.0	147

REFERENCES

- Aaronson, M. Huchra, J., Mould, J., Schechter, P., & Tully, R. B. 1982, *Astrophys. J.* 258, 64
- Bertschinger, E., Dekel, A., Faber, S. M., Dressler, A., & Burstein, D. 1990 *Astrophys. J.* 364, 370
- Bond, J. R. 1995, *Phy. Rev. Lett.*, 74, 4369
- Bucher, M. & Turok, N. 1995 preprint, hep-ph/9503393
- Bunn, T. 1995, Ph.D thesis, UC Berkeley
- Connolly, A. J., Szalay, A. S., & Bershad, M. A., Kinney, A. L. *et al.* 1995, *Astron. J.*, 110, 1071
- Davis, M., Strauss, M., & Yahil, A. 1991 *Astrophys. J.* 372, 394
- Davis, M., & Nusser, A. 1995, in *The Maryland Meeting on Dark Matter*, AIP Conference Proceedings 336, ed S. Holt & C. Bennett, p. 361
- Davis, M., Tonry, J., Huchra, J., & Latham, D. 1980, *Astrophys. J. (Lett.)* 238, L113
- Dekel, A. 1994, *Ann. Rev. of A & A*, **32**, 371
- Dekel, A. 1995, private comm.
- Dekel, A., Bertschinger, E., & Faber, S. M. 1990, *Astrophys. J.* 364, 349
- Dekel, A., Bertschinger, E., Yahil, A., Strauss, M., Davis, M., & Huchra, J. 1993, *Astrophys. J.* 412, 1
- Dressler, A. 1994, in *Cosmic Velocity Fields*, ed. F.R. Bouchet & M. Lachièze-Rey, Editions Frontières, p. 9
- Faber, S. & Burstein, D. 1988 in *Large Scale Motions in the Universe*, Princeton Univ. Press, ed. V Rubin & G Coyne, p. 115
- Fisher, K.B., Davis, M., Strauss, M.A., Yahil, A., & Huchra, J.P. 1994a, *M.N.R.A.S.* 267, 927.
- Fisher, K.B., Huchra, J., Strauss, M.A., Davis, M., Yahil, A., & Schlegel, D. 1995a, *Astrophys. J. (suppl.)* 100, 69
- Fisher, K.B., Lahav, O., Hoffman, Y., Lynden-Bell, D., & Zaroubi, S. 1995b, *M.N.R.A.S.* 272, 885
- Fisher, K.B., Scharf, C.A., & Lahav, O., 1994b, *M.N.R.A.S.* 266, 219
- Freudling, W., & da Costa, L., in *Cosmic Velocity Fields*, ed. F.R. Bouchet & M. Lachièze-Rey, Editions Frontières, p. 187.
- Gorski, K., Davis, M., Strauss, M., White, S., & Yahil, A. 1989 *Astrophys. J.* 344, 1

- Gorski, K. 1994, *ApJL.* , 430, L85
- Hudson, M. 1994, *M.N.R.A.S.* 266, 475
- Hudson, M.J., Dekel, A., Courteau, S., Faber, S.M., & Willick, J.A. 1995, *M.N.R.A.S.* 274, 305
- Jackson, D. 1962, *Classical Electrodynamics* Wiley
- Jacoby, G. H., Branch, D., Ciardullo, R., Davies, R. L., *et al.* 1992, *Pub. A. S. Pacific*, 104, 599
- Kaiser, N. 1987, *M.N.R.A.S.* 227, 1
- Kauffman, G., Nusser, A., & Steinmetz, M. 1996, *M.N.R.A.S.* in press.
- Kolatt T., Dekel, A., Ganon, G., & Willick J 1996, *Astrophys. J.* 458, 419
- Kraan-Korteweg, R.C., Woudt, P.A., Cayatte, V., Fairall, A.P., Balkowski, C., & Henning, P.A. 1996, *Nature*, 379, 519
- Kraan-Korteweg, R.C., Loan, A. J., Burton, W.B., Lahav, O. *et al.* 1994, *Nature*, 372, 77
- Lahav, O. 1991 in *Highlights of Astronomy*, vol.9, ed. Bergeron, J., Kluwer, Dordrecht
- Liddle, A.R. & Lyth, D.H. 1993, *Physics Reports*, 231, 1
- Lynden-Bell, D. 1991, in *Statistical Challenges in Modern Cosmology*, eds. Babu, G.B & Feigelson, E.D.
- Lynden-Bell, D., Faber, S. M., Burstein, D., Davies, R. L., Dressler, A., Terlevich, R. J., & Wegner, G. 1988, *Astrophys. J.* 326, 19
- Miller, A., Davis, M., & White, S.D.M. 1996, preprint
- Nusser, A., & Davis, M. 1994, *Astrophys. J. (Lett.)* 421, L1
- Nusser, A., & Davis, M. 1995, *M.N.R.A.S.* 276, 1391
- Nusser, A., Dekel, A., Bertschinger, E., & Blumenthal, G. R. 1991, *Astrophys. J.* 379, 6
- Ostriker, J, Peebles, P.J.E, & Yahil, A. 1974, *Astrophys. J. (Lett.)* 193, L1
- Peebles, P. J. E. 1980, *The Large Scale Structure of the Universe*, Princeton Press, p. 65
- Peebles, P. J. E. 1992, in *Relativistic Astrophysics and Particle Cosmology*, Texas/PASCOS 92 Symp. ed C. W. Akerlof & M. A. Srednicki (Ann. NY Acad Sci. vol 688), 84
- Press, W.H., Teukolsky, S.A., Vetterling, W.T., & Flannery, B.P. 1992, *Numerical Recipes*, (Second Edition) Cambridge University Press
- Regös, E., & Szalay, A. 1989, *Astrophys. J.* 345, 627
- Roth, J. 1993, in *Cosmic Velocity Fields*, ed. F. Bouchet & M. Lachieze-Rey, Editions Frontieres, p233.

- Schechter, P. 1980 *Astrophys. J.* 85, 801
- Schlegel, D., Davis, M., Summers, F., & Holtzman, J. A. 1994, *Astrophys. J.* 427 527
- Schlegel, D, Finkbeiner, D, & Davis, M. 1996, in preparation
- Strauss, M. A., & Davis, M. 1988, in *Large Scale Motions in the Universe*, ed. V Rubin & G Coyne, Princeton Univ. Press, p. 256
- Strauss, M.A., Davis, M., Yahil, A., & Huchra, J. 1992, *Astrophys. J.* 385, 421
- Strauss, M. A., & Willick, J. 1995, *Physics Reports*, 261, 271
- Strauss, M.A., Willick, J.A., Schlegel, D., Postman, M., & Courteau, S. 1996 in preparation
- Strauss, M.A., Yahil, A., Davis, M., Huchra, J.P., & Fisher, K. 1992 *Astrophys. J.* 397, 395
- Therrien, C. W. 1992, *Discrete Random Signal and Statistical Signal Processing*, (New Jersey: Prentice-Hall)
- Tonry, J, & Davis, M. 1981 *Astrophys. J.* 246, 680
- Tonry, J, & Dressler, A. 1995, in preparation
- Vogeley, M. S. , & Szalay, A. S. 1996, preprint astro-ph/9601185
- Willick, J.A. 1990, *Astrophys. J. (Lett.)* 351, L5
- Willick, J.A. 1994, *Astrophys. J. (suppl.)* 92, 1.
- Willick, J.A., Courteau, S, Faber, S., Burstein, D., *et al.* 1995, *Astrophys. J.* 446, 12
- Willick, J.A., Courteau, S, Faber, S., Burstein, D., Dekel, A., & Kolatt, T. 1996a, *Astrophys. J.* 457, 460
- Willick, J.A. *et al.* 1996b, in preparation
- Willick, J.A. *et al.* 1996c, in preparation
- Yahil, A. 1988, in *Large Scale Motions in the Universe*, Princeton Univ. Press, ed. V Rubin & G Coyne, p. 219
- Yahil, A., Strauss, M. A., Davis, M., & Huchra, J. 1991 *Astrophys. J.* 372, 380

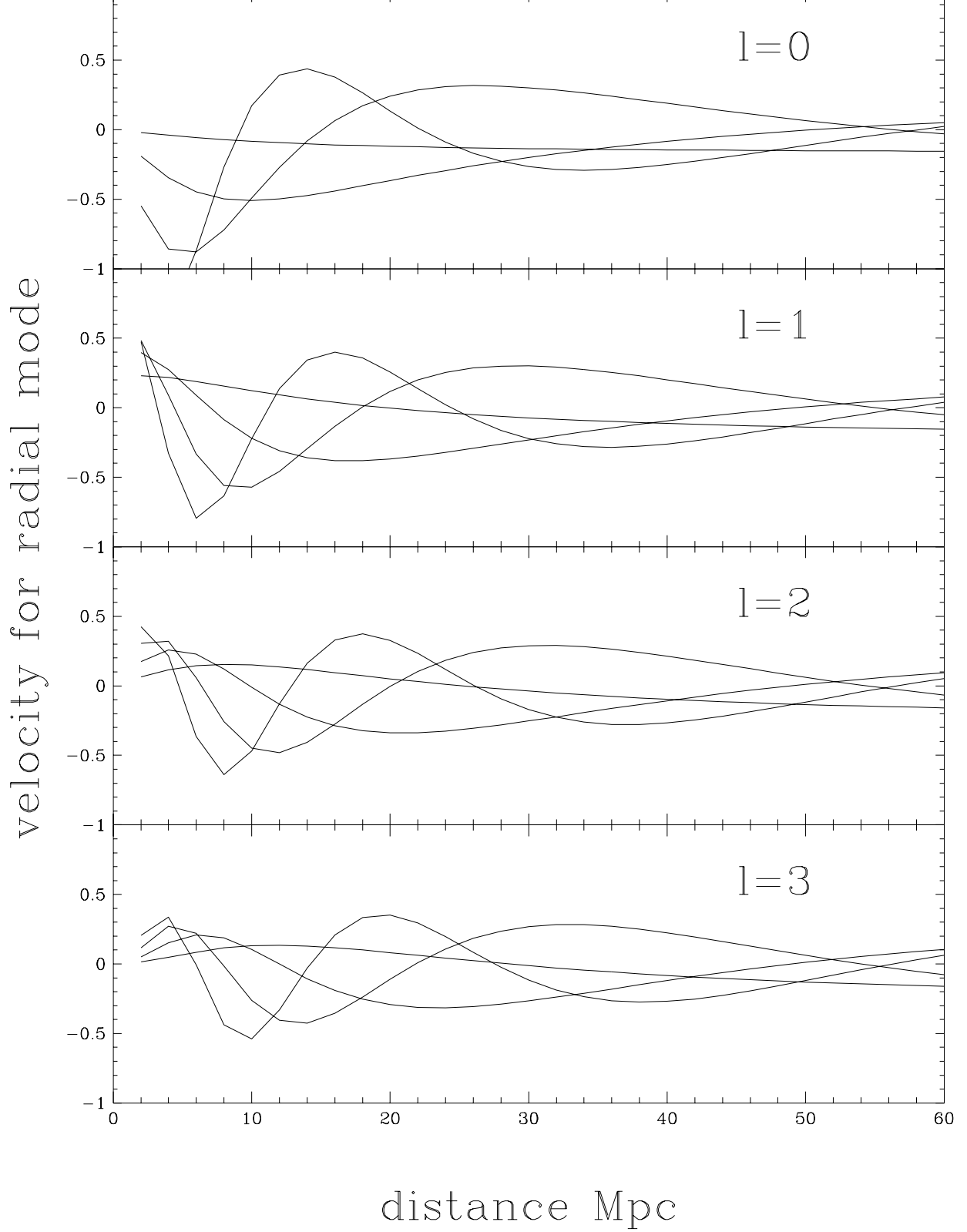


Figure 1: The amplitude of the radial variation of the mode velocities versus cz for $l=0-3$. Note that the radial resolution drops sharply with redshift.

this figure available by anonymous ftp at [magicbean.berkeley.edu/pub/marc/m3itf/](ftp://magicbean.berkeley.edu/pub/marc/m3itf/)

Figure 2: The u_{itf} sky projection as seen in the LG frame for the mock catalog, in galactic coordinates. The open circles are points that are flowing inward and the stars are points flowing outward. The size of the symbols is proportional to the flow velocity, with a key showing 500 km s^{-1} flow. Note the three separate panels of redshift interval. Note also the dominance of the dipole mode, especially for the outer shell. This is the signature of the reflex motion of the LG.

this figure available by anonymous ftp at [magicbean.berkeley.edu/pub/marc/m3itf/](ftp://magicbean.berkeley.edu/pub/marc/m3itf/)

Figure 3: The u_{itf} field for points within 30° of the Supergalactic Plane, plotted in this plane, for the mock catalog, in the LG frame. Solid symbols and solid lines are outflowing “galaxies” with the symbol drawn at the distance and the line drawn to the measured LG redshift. Open symbols and dashed lines correspond to “galaxies” infalling to the LG. Note again the strong dipole pattern of the flow at $z > 3000 \text{ km s}^{-1}$.

this figure available by anonymous ftp at magicbean.berkeley.edu/pub/marc/m3itf/

Figure 4: (a) The true, unfiltered peculiar velocities, u_{true} of the points in the mock catalog, plotted in the Supergalactic Plane. (b:) The true peculiar velocities, u_{true}^f of the mock catalog points, after filtering by the 56 mode expansion. Note how the large scale behavior of panel a is reproduced in panel b. The high spatial frequency signal, which is very difficult to reproduce in the *IRAS* gravity field, is effectively eliminated in Figure 4b. (c:) The *IRAS* predicted velocity field for the mock catalog, u_{iras} , plotted in the Supergalactic Plane. (d:) The same as panel (c), but now filtered by the 56 mode expansion, u_{iras}^f .

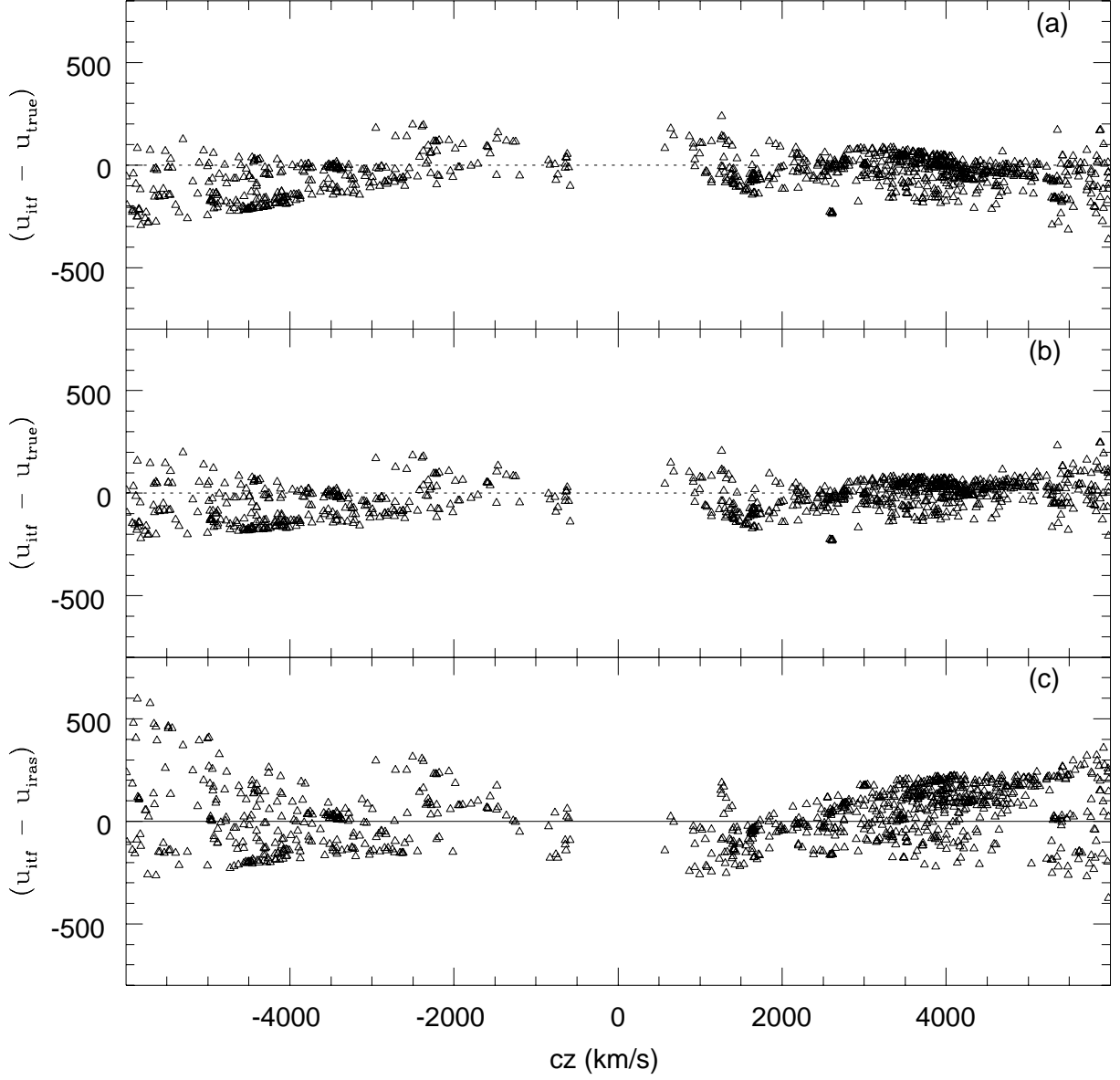


Figure 5: (a:) The residuals $u_{itf} - u_{true}^f$ as a function of cz of points in the mock catalog within 60° of the apex and anti-apex direction $(l,b) = (270,30)$, before correction for the bias in the slope parameter γ . (b:) The same plot $u_{itf} - u_{true}^f$ after the bias in the slope parameter is removed. (c:) The residuals of $u_{itf} - u_{iras}^f$ for the same galaxies.

this figure available by anonymous ftp at [magicbean.berkeley.edu/pub/marc/m3itf/](ftp://magicbean.berkeley.edu/pub/marc/m3itf/)

Figure 6a: Residuals $u_{itf} - u_{true}^f$, in sky slices for mock catalog, using the same notation as in Figure 2.

this figure available by anonymous ftp at [magicbean.berkeley.edu/pub/marc/m3itf/](ftp://magicbean.berkeley.edu/pub/marc/m3itf/)

Figure 6b: Residuals $u_{itf} - u_{iras}^f$ in the same projection. Note the small amplitude of these residuals versus Figure 2, and the absence of significant dipole contribution to these residuals. Note that the amplitude of the residuals in (6b) are somewhat larger than those of (6a), because of the *IRAS* contributed noise.

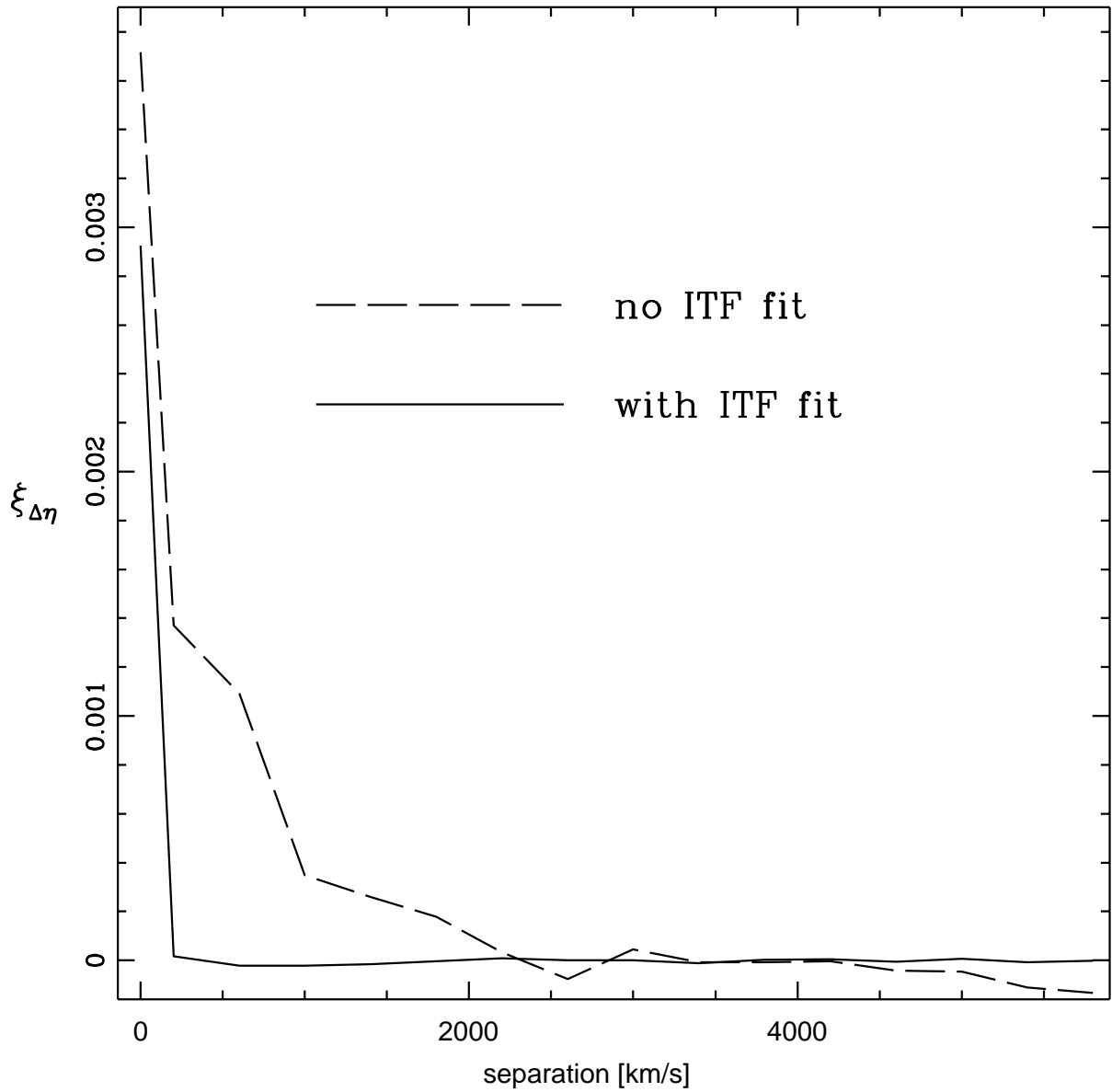


Figure 7: The auto-correlation function of the η residuals of the Mark III galaxies versus redshift space separation. The dashed curve results when the 56 mode coefficients are set to 0, while the solid curve is after the 56 modes are fit to the Mark III data.

this figure available by anonymous ftp at [magicbean.berkeley.edu/pub/marc/m3itf/](ftp://magicbean.berkeley.edu/pub/marc/m3itf/)

Figure 8: The ITF velocity field u_{itf} for the Mark III galaxies using the same sky projection as Figure 2.

this figure available by anonymous ftp at [magicbean.berkeley.edu/pub/marc/m3itf/](ftp://magicbean.berkeley.edu/pub/marc/m3itf/)

Figure 9: The ITF velocity field u_{itf} : for Mark III galaxies within 30° of the supergalactic plane, using the same notation as in Figure 3.

this figure available by anonymous ftp at [magicbean.berkeley.edu/pub/marc/m3itf/](ftp://magicbean.berkeley.edu/pub/marc/m3itf/)

Figure 10: The sky projection of the *IRAS* predicted flow field u_{iras} for $\beta = 0.4$ for the Mark III galaxies.

this figure available by anonymous ftp at [magicbean.berkeley.edu/pub/marc/m3itf/](ftp://magicbean.berkeley.edu/pub/marc/m3itf/)

Figure 11: The supergalactic plane projection for the *IRAS* predicted flow field u_{iras} for $\beta = 0.4$ for the Mark III galaxies.

this figure available by anonymous ftp at [magicbean.berkeley.edu/pub/marc/m3itf/](ftp://magicbean.berkeley.edu/pub/marc/m3itf/)

Figure 12: The sky projection of the residuals $u_{itf} - u_{iras}$ for $\beta = 0.4$. This is simply the difference between Figures 8 and 10. Compare this field to Figure 6b.

this figure available by anonymous ftp at [magicbean.berkeley.edu/pub/marc/m3itf/](ftp://magicbean.berkeley.edu/pub/marc/m3itf/)

Figure 13: The same as Figure 12, now for $\beta = 0.7$.

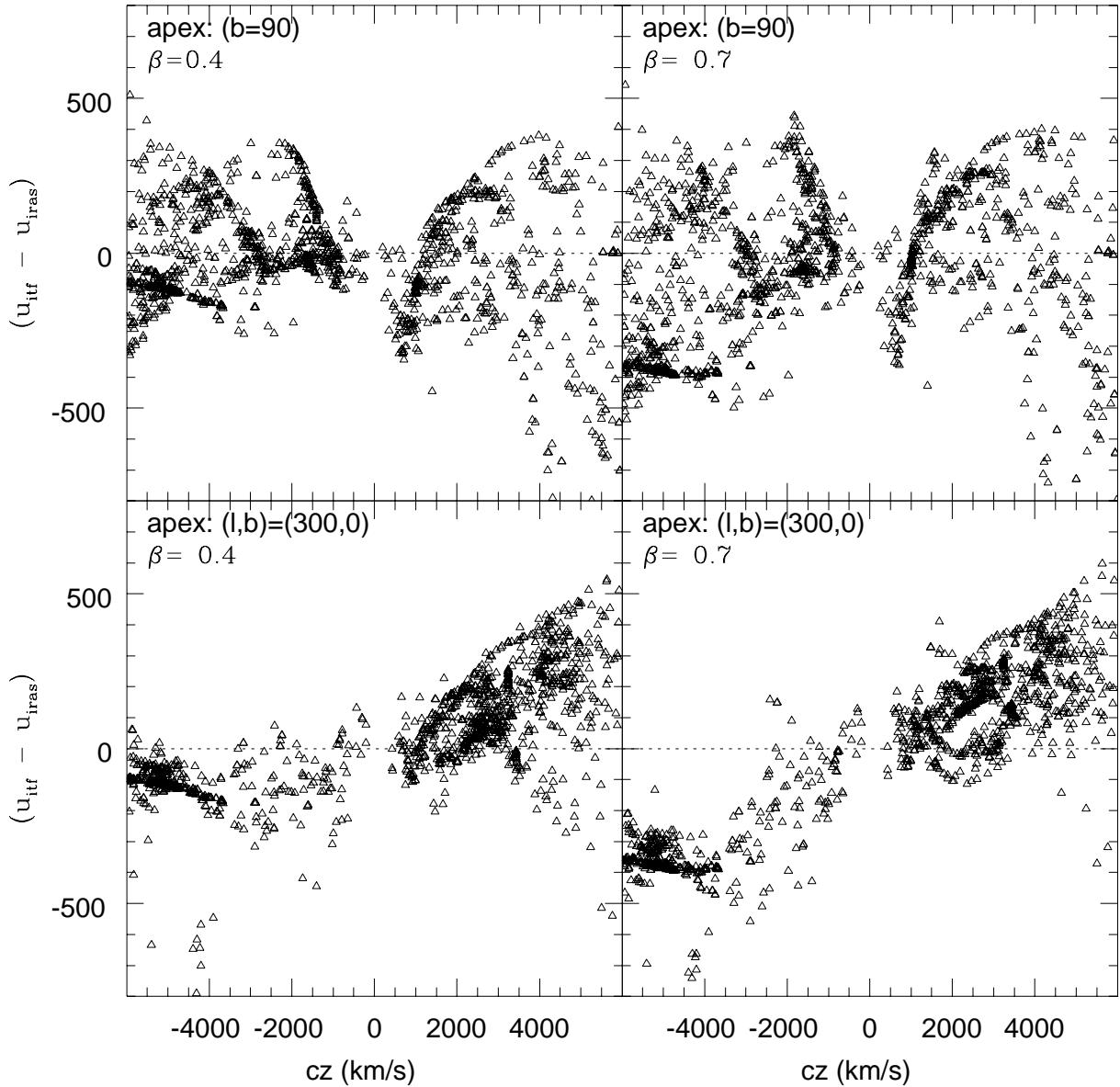


Figure 14: (left): The residual $u_{itf} - u_{iras}$ of all points within 60° of the apex and antiapex of $(l,b) = (0,90)$ and $(300,0)$, for $\beta = 0.4$. (right) The same residual for the case $\beta = 0.7$. Note the linearly growing dipole residual toward $(300,0)$.

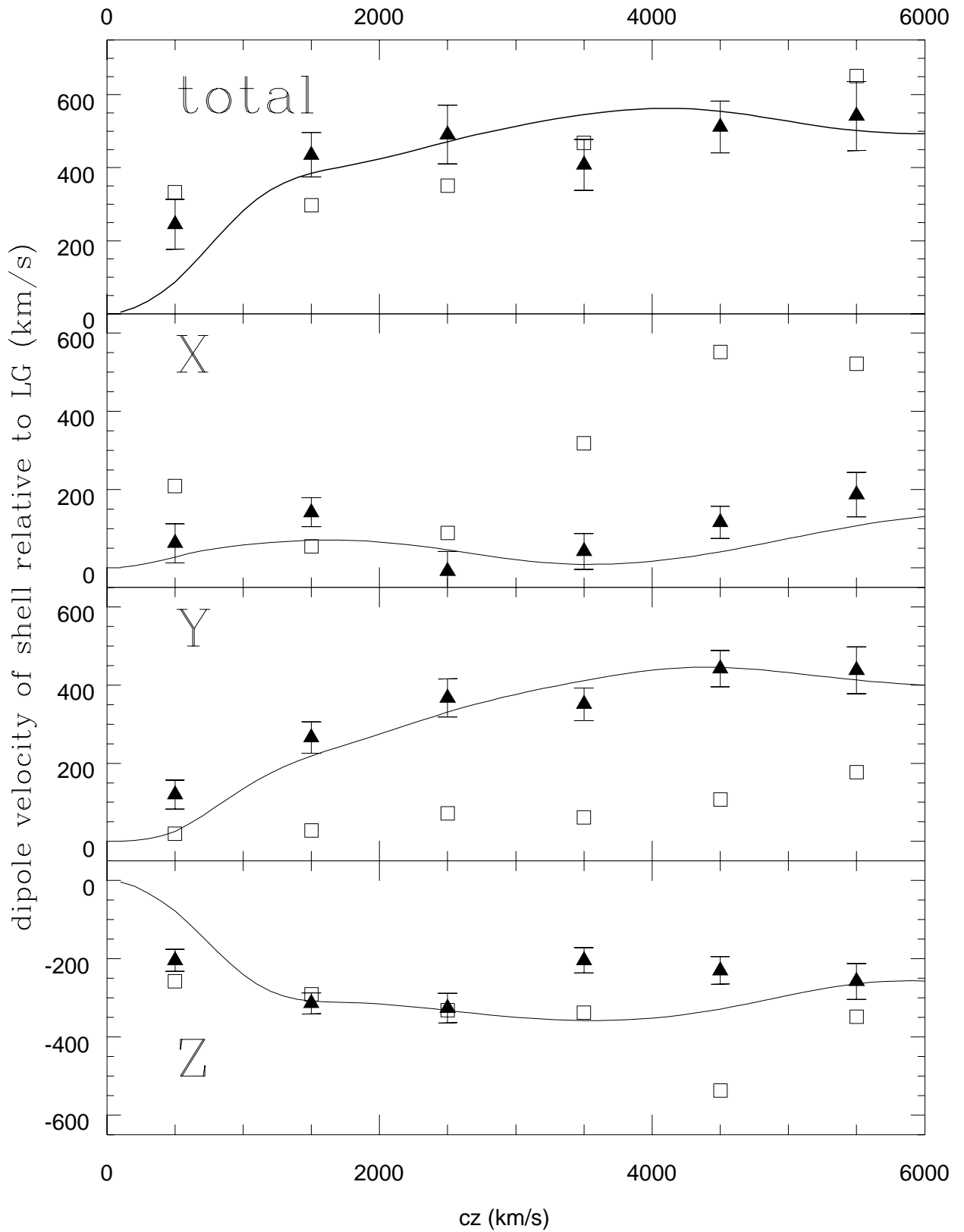


Figure 15: The dipole field derived from the Mark III galaxies. The ITF dipole is plotted as the open symbols, while the *IRAS* dipole for $\beta = 0.6$ is plotted as the closed symbols. The X,Y,Z panels show the three Galactic components of the dipole and the top panel is their quadrature sum. The solid line is the full *IRAS* dipole field calculated from Equation 4. The Mark III galaxies are binned in redshift shells of 1000 km s^{-1} thickness. Note that the *IRAS* inferred dipole for the Mark III symbols tracks the solid line, while the X and Y components of the ITF dipole are quite deviant from the line.

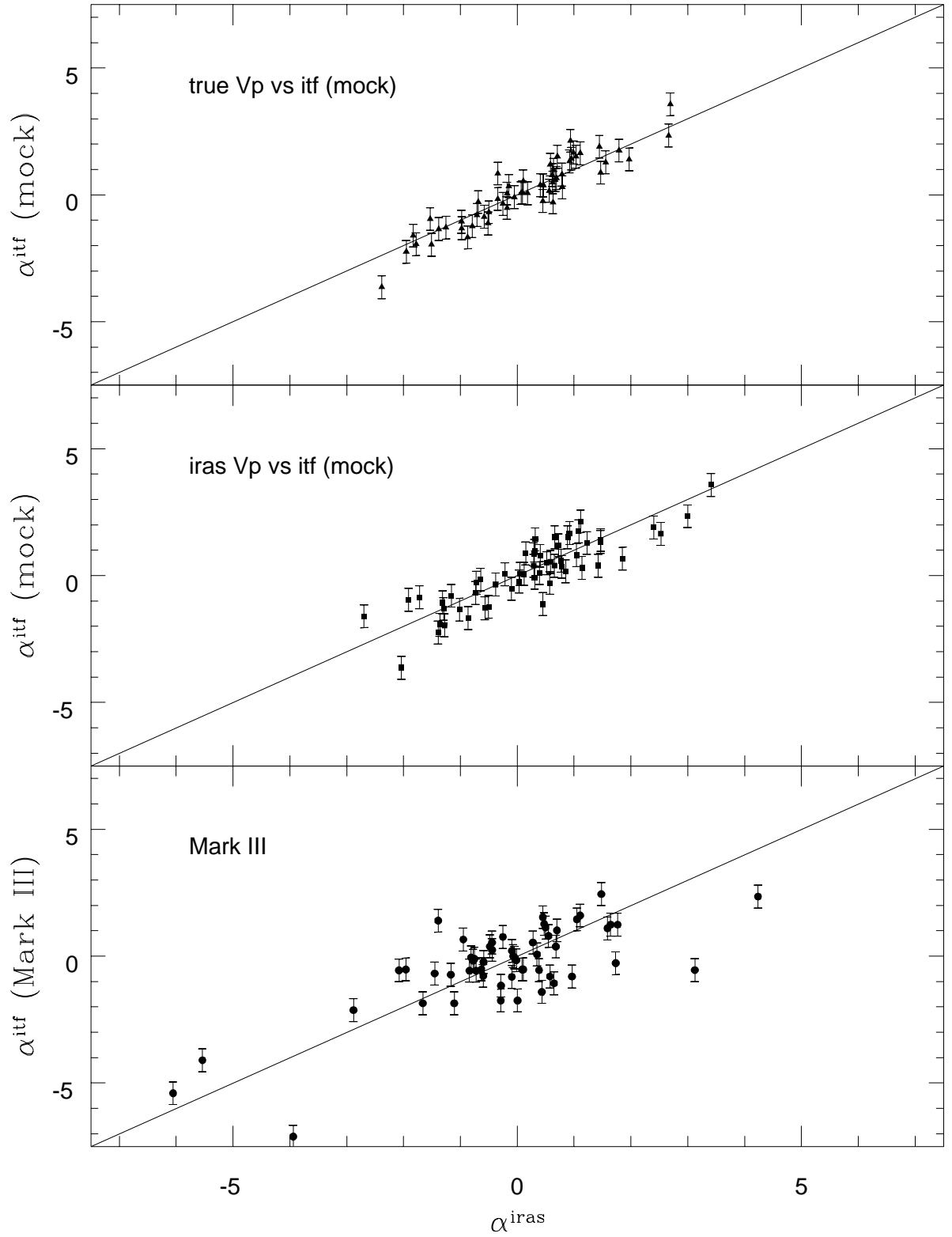


Figure 16: (top:) A scatter diagram of α^{itf} versus the true coefficients α^{true} for the mock catalog. The ITF errors are shown. (middle:) Scatter of α^{itf} versus α^{iras} for the mock catalog. The increased scatter is induced by the errors in α^{iras} , not shown because of the covariance. (bottom:) The scatter of α^{itf} versus α^{iras} for the real Mark III data ($\beta = 0.6$). Note the qualitative agreement of the mode amplitudes but the further increase in scatter.